Editors' Suggestion | Featured in Physics

Hyper Suprime-Cam Year 3 results: Cosmology from galaxy clustering and weak lensing with HSC and SDSS using the minimal bias model

Sunao Sugiyama,[1,2,*] Hironao Miyatake,[3,4,1] Surhud More,[5,1] Xiangchong Li,[6,1] Masato Shirasaki,[7,8] Masahiro Takada,[1] Yosuke Kobayashi,[9,1] Ryuichi Takahashi,[10] Takahiro Nishimichi,[11,1,12] Atsushi J. Nishizawa,[13,14] Markus M. Rau,[6,15] Tianqing Zhang,[6] Roohi Dalal,[16] Rachel Mandelbaum,[6] Michael A. Strauss,[16] Takashi Hamana,[17] Masamune Oguri,[18,19,2,1] Ken Osato,[20,21] Arun Kannawadi,[16] Bau-Ching Hsieh,[22] Wentao Luo,[23,24] Robert Armstrong,[25] James Bosch,[16] Yutaka Komiyama,[26] Robert H. Lupton,[16] Nate B. Lust,[16] Satoshi Miyazaki,[27] Hitoshi Murayama,[28,29,1] Yuki Okura,[17] Paul A. Price,[16] Philip J. Tait,[27] Masayuki Tanaka,[17] and Shiang-Yu Wang[22]

[1]*Kavli Institute for the Physics and Mathematics of the Universe (WPI), The University of Tokyo Institutes for Advanced Study (UTIAS), The University of Tokyo, Chiba 277-8583, Japan*
[2]*Department of Physics, The University of Tokyo, Bunkyo, Tokyo 113-0031, Japan*
[3]*Kobayashi-Maskawa Institute for the Origin of Particles and the Universe (KMI), Nagoya University, Nagoya, 464-8602, Japan*
[4]*Institute for Advanced Research, Nagoya University, Nagoya 464-8601, Japan*
[5]*The Inter-University Centre for Astronomy and Astrophysics, Post bag 4, Ganeshkhind, Pune 411007, India*
[6]*McWilliams Center for Cosmology, Department of Physics, Carnegie Mellon University, Pittsburgh, Pennsylvania 15213, USA*
[7]*National Astronomical Observatory of Japan, Mitaka, Tokyo 181-8588, Japan*
[8]*The Institute of Statistical Mathematics, Tachikawa, Tokyo 190-8562, Japan*
[9]*Department of Astronomy/Steward Observatory, University of Arizona, 933 North Cherry Avenue, Tucson, Arizona 85721-0065, USA*
[10]*Faculty of Science and Technology, Hirosaki University, 3 Bunkyo-cho, Hirosaki, Aomori 036-8561, Japan*
[11]*Center for Gravitational Physics and Quantum Information, Yukawa Institute for Theoretical Physics, Kyoto University, Kyoto 606-8502, Japan*
[12]*Department of Astrophysics and Atmospheric Sciences, Faculty of Science, Kyoto Sangyo University, Motoyama, Kamigamo, Kita-ku, Kyoto 603-8555, Japan*
[13]*Gifu Shotoku Gakuen University, Gifu 501-6194, Japan*
[14]*Institute for Advanced Research/Kobayashi Maskawa Institute, Nagoya University, Nagoya 464-8602, Japan*
[15]*High Energy Physics Division, Argonne National Laboratory, Lemont, Illinois 60439, USA*
[16]*Department of Astrophysical Sciences, Princeton University, Princeton, New Jersey 08544, USA*
[17]*National Astronomical Observatory of Japan, National Institutes of Natural Sciences, Mitaka, Tokyo 181-8588, Japan*
[18]*Center for Frontier Science, Chiba University, 1-33 Yayoi-cho, Inage-ku, Chiba 263-8522, Japan*
[19]*Research Center for the Early Universe, The University of Tokyo, Bunkyo, Tokyo 113-0031, Japan*
[20]*Center for Frontier Science, Chiba University, Chiba 263-8522, Japan*
[21]*Department of Physics, Graduate School of Science, Chiba University, Chiba 263-8522, Japan*
[22]*Academia Sinica Institute of Astronomy and Astrophysics, No. 1, Sec. 4, Roosevelt Rd., Taipei 10617, Taiwan*
[23]*School of Physical Sciences, University of Science and Technology of China, Hefei, Anhui 230026, China*
[24]*CAS Key Laboratory for Researches in Galaxies and Cosmology/Department of Astronomy, School of Astronomy and Space Science, University of Science and Technology of China, Hefei, Anhui 230026, China*
[25]*Lawrence Livermore National Laboratory, Livermore, California 94551, USA*
[26]*Department of Advanced Sciences, Faculty of Science and Engineering, Hosei University, 3-7-2 Kajino-cho, Koganei-shi, Tokyo 184-8584, Japan*
[27]*Subaru Telescope, National Astronomical Observatory of Japan, 650 N Aohoku Place, Hilo, Hawaii 96720, USA*
[28]*Berkeley Center for Theoretical Physics, University of California, Berkeley, California 94720, USA*
[29]*Theory Group, Lawrence Berkeley National Laboratory, Berkeley, California 94720, USA*

[*]sunao.sugiyama@ipmu.jp

(Received 6 April 2023; accepted 22 June 2023; published 11 December 2023)

We present cosmological parameter constraints from a blind joint analysis of three two-point correlation functions measured from the Year 3 Hyper Suprime-Cam (HSC-Y3) imaging data, covering about 416 deg^2, and the SDSS DR11 spectroscopic galaxies spanning the redshift range [0.15, 0.70]. We subdivide the SDSS galaxies into three luminosity-cut, and therefore nearly volume-limited samples separated in redshift, each of which acts as a large-scale structure tracer characterized by the measurement of the projected correlation function, $w_{\rm p}(R)$. We also use the measurements of the galaxy-galaxy weak-lensing signal $\Delta\Sigma(R)$ for each of these SDSS samples which act as lenses for a secure sample of source galaxies selected from the HSC-Y3 shape catalog based on their photometric redshifts. We combine these measurements with the cosmic shear correlation functions, $\xi_{\pm}(\vartheta)$ measured for our HSC source sample. We model these observables with the minimal bias model of the galaxy clustering observables in the context of a flat ΛCDM cosmology. We use conservative scale cuts, $R > 12$ and $8h^{-1}$ Mpc for $\Delta\Sigma$ and $w_{\rm p}$, respectively, where the minimal bias model is valid, in addition to conservative prior on the residual bias in the mean redshift of the HSC photometric source galaxies. We present various validation tests of our model as well as analysis methods. Our baseline analysis yields $S_8 = 0.775^{+0.043}_{-0.038}$ (68% C.I.) for the ΛCDM model, after marginalizing over uncertainties in other parameters. Our value of S_8 is consistent with that from the *Planck* 2018 data, but the credible interval of our result is still relatively large. We show that various internal consistency tests based on different splits of the data are passed. Our results are statistically consistent with those of a companion paper, which extends this analysis to smaller scales with an emulator-based halo model, using $\Delta\Sigma(R)$ and $w_{\rm p}(R)$ down to $R > 3$ and $2h^{-1}$ Mpc, respectively.

DOI: 10.1103/PhysRevD.108.123521

I. INTRODUCTION

Wide-area imaging surveys are powerful tools for constraining the composition of the Universe and the growth history of cosmic structure. Motivated by this fact, the international Subaru Hyper Suprime-Cam (HSC) collaboration consisting of scientists mainly from Japan, Taiwan, and Princeton University has carried out a wide-area, multiband imaging survey with HSC, covering about $1,100$ deg^2 [1,2]. In particular, comparing the measurements of weak-lensing effects due to large-scale structure in the Universe with predictions from cosmological models allows us to obtain precise estimates of cosmological parameters [3–8]. Interestingly, however, the majority of large-scale structure probes infer a lower value of σ_8 or $S_8 \equiv \sigma_8(\Omega_{\rm m}/0.3)^{0.5}$, a parameter that characterizes the amplitude of the matter clustering on scales of $8h^{-1}$ Mpc in the Universe today, compared to that inferred from the *Planck* cosmic microwave background data [9], albeit at low statistical significance. If established at high statistical significance, and after ruling out any systematic biases as an origin, this so-called σ_8 or S_8 tension (see [10] for a review) might be a consequence of new physics beyond the standard ΛCDM model of the Universe.

Establishing or ruling out the S_8 tension with cosmological datasets is, therefore, one of the most important contemporary problems in modern cosmology. To do this, we require high-precision, robust cosmology experiments. Here by "high-precision", we mean experiments yielding small credible intervals (small error bars) on the cosmological parameter of interest, here S_8, and by "robust", we mean experiments that can provide an unbiased estimate of the underlying true value of S_8. This is the direction the cosmology community is heading in the coming decade.

In this paper, we model measurements from the Year 3 galaxy shape catalog of Subaru HSC (hereafter HSC-Y3) and the spectroscopic SDSS DR11 galaxy catalog, to perform a joint cosmological analysis of galaxy clustering, galaxy-galaxy clustering and cosmic shear—a 3×2pt analysis. This paper is an extension of Sugiyama *et al.* [6] which used the Year 1 HSC (HSC-Y1) data of about 140 deg^2 to perform a joint cosmological analysis of galaxy clustering and galaxy-galaxy weak-lensing (2×2pt) analysis. In this paper, we use the HSC-Y3 catalog covering about 416 deg^2, which is approximately three times larger area than in HSC-Y1, and supplement the 2×2pt measurements with the cosmic shear correlation functions to perform a joint analysis.

The main challenge in the use of galaxy clustering for cosmological analyses lies in the relation between the distribution of galaxies and that of matter (mainly dark matter) in the large-scale structure—the so-called galaxy bias uncertainty [11] (also see [12] for a review). Observationally, galaxy-galaxy weak lensing, measured from the cross-correlation of the positions of lens galaxies with shapes of background galaxies, can be used to measure the average matter distribution around lens galaxies, which, in turn, can be used to infer the galaxy bias

when combined with the autocorrelation of galaxies in the lens sample [5,13,14].

In order to carry out a cosmological analysis, we need a theoretical model to describe our observables. However, it is still very challenging to accurately model the galaxy bias and its scale dependence from first principles due to complex physical processes that are inherent to the formation and evolution of galaxies. Cosmological perturbation theory [12,15] provides an accurate modeling framework to describe the clustering properties of galaxies. In this paper, we utilize the minimal bias model to describe the galaxy clustering observables. In this model, we model the autocorrelation function of galaxies as $\xi_{\rm gg}(r) = b_1^2\xi_{\rm mm}^{\rm NL}(r)$ and the cross-correlation function of matter and galaxies as $\xi_{\rm gm}(r) = b_1\xi_{\rm mm}^{\rm NL}(r)$, where b_1 is a linear bias parameter and $\xi_{\rm mm}^{\rm NL}(r)$ is the nonlinear correlation function of matter. The galaxy-galaxy weak-lensing and the projected galaxy clustering correlation function probe the line-of-sight projection of $\xi_{\rm gm}(r)$ and $\xi_{\rm gg}(r)$, respectively. Their combination allows us to break degeneracies between b_1 and $\xi_{\rm mm}^{\rm NL}$, the latter of which allows us to extract the cosmological information. On sufficiently large length scales, where gravity is the driving dominant force for structure formation and local baryonic physics do not affect the observables, the minimal bias model serves as a phenomenologically accurate theoretical framework that can be applied to any galaxy type. However, the model breaks down on smaller scales where a complex, scale-dependent galaxy bias appears.

The purpose of this paper is to obtain robust cosmological constraints from the 3×2pt cosmological analysis using the minimal galaxy bias model and flat ΛCDM cosmological model. We use the galaxy-galaxy weak lensing and the projected correlation function of galaxies measured on conservatively-chosen scales, where the minimal bias model is safely valid. Furthermore, we will show that the addition of the cosmic shear correlation function can improve the cosmological constraints when combined with the 2×2pt measurements. We will present various validation tests of the minimal bias model using mock 2×2pt signals that include different galaxy bias models and other physical systematic effects. In addition, we employ a nuisance parameter to model a possible residual ensemble photometric redshift (hereafter photo-z) error in the HSC source galaxies that are used for the measurements and model of galaxy-galaxy weak-lensing and cosmic shear signals, because ensemble photo-z errors are one of the most important systematic effects in weak-lensing measurements. A companion paper, Miyatake *et al.* [16], indicates a nonzero residual photo-z error from the analysis of the same weak-lensing data as is used in this paper. We will also perform various internal consistency tests to check that our results remain consistent across various splits of the data.

This paper is a companion paper to More *et al.* [17] and Miyatake *et al.* [16]. The measurements, systematics and covariance estimates for the 3×2pt signals are described in More *et al.* [17] These signals are analyzed using two different models in Miyatake *et al.* [16] and in this paper. In the former case, we model the measured signals down to smaller scales using an emulator-based halo-model framework, where the galaxy bias is determined as an average over the bias of halos weighted by the halo-occupation probability of galaxies. The additional degrees of freedom in the halo occupation distribution make it possible to model the signals on scales below those used in this paper [14,16]. The results presented in this paper are thus complementary to those in the companion paper, Miyatake *et al.* [16], which uses an emulator-based halo model to estimate the cosmological parameters from the same observables as those used in this paper, but down to smaller scales. We will show that the results using different theoretical models are consistent with each other. This consistency strengthens our confidence in the cosmological parameters inferred from our analyses, in particular that the results are robust against contamination from possible baryonic effects inherent in physical processes of galaxy formation and evolution (including the assembly bias effect).

In addition, there are two more companion papers, Li *et al.* [18] and Dalal *et al.* [19] that perform cosmological parameter analyses using the real- and Fourier-space tomographic cosmic shear analyses of the HSC-Y3 data, respectively. The two 3×2pt analyses use the same blinded catalog (as they use the same measurements but on different scales), while the two cosmic shear analyses use entirely independent blinded catalogs. These cosmological analyses were led by different authors without comparing the cosmological parameter results until after each analysis was unblinded. We present the results without any change after unblinding; any results or conclusions derived post-unblinding are mentioned explicitly in the paper. For all these analyses, we employ a conservative prior on any residual errors on the true ensemble redshift distribution of HSC galaxies beyond $z \gtrsim 0.7$ to model possible residual photo-z errors. All of these analysis choices were defined during the blind phase of the analysis.

This paper is organized as follows. In Sec. II, we briefly describe the data and measurement methods. In Sec. III, we describe the theoretical model that we use to infer cosmological parameters for the flat ΛCDM model, our choice of model for systematic effects, and the likelihood analysis method. In Sec. IV, we describe the strategy we adopt to perform a blind analysis. In Sec. V, we perform model validation using different types of mock data vectors. In Sec. VI we show the cosmological parameters inferred from our 3×2pt analysis. Section VII is devoted to conclusions and a discussion of our results.

II. DATA AND MEASUREMENT

In this section we briefly describe the data and the measurement methods. The details can be found in a companion paper, More *et al.* [17].

A. HSC-Y3 data: Source galaxies for weak lensing

HSC is a wide-field prime focus camera on the 8.2m Subaru Telescope [1,20–22]. The HSC Subaru Strategic Program (HSC SSP) survey started in 2014, and used 330 Subaru nights to conduct a five-band (*grizy*) wide-area imaging survey [2]. The combination of HSC's wide field-of-view (1.77 $\deg^2$), superb image quality (a median i-band seeing FWHM of $0.6''$), and large photon-collecting power makes it one of the most powerful instruments for weak-lensing measurements. The HSC SSP survey consists of three layers; Wide, Deep, and Ultradeep. The Wide layer, which is designed for weak-lensing cosmology, covers about $1,100$ $\deg^2$ of the sky with a 5σ depth of $i \sim 26$ ($2''$ aperture for a point source). Since the i-band images are used for galaxy-shape measurements in weak-lensing analyses, they are preferentially taken under good seeing conditions.

In this paper, we use the HSC three-year (hereafter HSC-Y3) galaxy-shape and photo-z catalogs [23,24] constructed from about 90 nights of HSC Wide data taken between March 2014 and April 2019. Both catalogs are based on the object catalog produced by the data reduction pipeline [25]. In the following subsections, we describe details of the shape and photo-z catalogs.

1. HSC-Y3 galaxy-shape catalog

In this paper, we use the shape catalog from the S19a internal data release which was processed with hscPipe v7 [26]. There were a number of improvements to the PSF modelling, image warping kernel, background subtraction and bright star masks, which have improved the quality of the shape catalog in Year 3 compared to the Year 1 shape catalog [23,24]. The detailed selection of galaxies that form the shape catalog is presented in Li *et al.* [26]. Briefly, the shape catalog consists of galaxies selected from the "full-depth full-color region" in all five filters. Apart from some basic quality cuts related to pixel level information, we select extended objects with an extinction corrected cmodel magnitude $i < 24.5$, i-band SNR ≥ 10, resolution > 0.3, $> 5\sigma$ detection in at least two bands other than i, a 1 arcsec diameter aperture magnitude cut of $i < 25.5$, and a blendedness cut in the i-band of $10^{-3.8}$.

The original shape catalog contains more than 35 million source galaxies covering 433 $\deg^2$. However, as described in detail in More *et al.* [17], Dalal *et al.* [19], Li *et al.* [18], we find a significant source of B-mode systematics in the cosmic shear correlation functions for a $\sim$20 $\deg^2$ patch in the GAMA09H region, and we remove this problematic region from the following analysis. After removing this $\sim$20 $\deg^2$ region, we have the HSC area of 416 $\deg^2$, with an effective weighted number density of 19.9 arcmin^{-2}. It is divided into six disjoint regions: the XMM, VVDS, GAMA09H, WIDE12H, GAMA15H, and HECTOMAP fields [see Fig. 2 in Ref. [26]]. The shape measurements in the catalog were calibrated using detailed image simulations, such that the residual galaxy property-dependent multiplicative shear estimation bias is less than $\sim 10^{-2}$. Li *et al.* [26] also present a number of systematic tests and null tests, and quantify the level of residual systematics in the shape catalog that could affect the cosmological science analyses carried out using the data. Given that Li *et al.* [26] flag residual additive biases due to PSF model shape residual correlations and star galaxy shape correlations as systematics requiring special attention and marginalization, we have included the effects of these systematics on the cosmic shear measurements in our modeling scheme.

2. Secure source galaxy sample definition

The depth of the HSC-Y3 data enables us to define a conservative sample of source galaxies that are at redshifts well beyond those of the lens galaxies, for weak-lensing measurements. In this paper we select three distinct samples of lens galaxies from the database of spectroscopic SDSS galaxies up to $z_{\mathrm{l,max}} = 0.7$. To select background galaxies, we use photometric redshift (hereafter photo-z) estimates for each HSC galaxy. The three year shape catalog is accompanied by a photometric redshift catalog of galaxies based on three different methods [27] MIZUKI is a template fitting-based photo-z estimation code. DEMPZ and DNNZ, on the other hand, provide machine learning-based estimates of the galaxy photo-z's. Each of these methods provides an estimate of the posterior distribution of redshift for each galaxy, denoted as $P(z_{\mathrm{s}})$. In this paper we use the DEMPZ photo-z catalog as our fiducial choice. Photo-z uncertainties are among the most important systematic effects in weak-lensing cosmology, and can cause significant biases in the cosmological parameters if unknown residual systematic errors in photo-z exist.

For the study of weak lensing, we define a sample of background galaxies whose redshifts are physically well beyond the maximum lens redshift $z_{\mathrm{l,max}}$. More specifically, we choose source galaxies satisfying the following condition [28–30]:

$$\int_{z_{\mathrm{l,max}}+0.05}^{7} P_i(z_{\mathrm{s}})\mathrm{d}z_{\mathrm{s}} \geq 0.99, \tag{1}$$

where the maximum redshift ($z_{\mathrm{l,max}} = 0.7$) is that of the lens sample that we will use for the galaxy-galaxy lensing measurements, and $P_i(z_{\mathrm{s}})$ is the posterior photo-z distribution for the ith HSC galaxy. Such cuts significantly reduce the contamination of source galaxies that are physically associated with the lens galaxies. With this additional cut, our weak-lensing sample includes about 24 percent of the galaxies in the original catalog, with an

effective number density of 4.9 galaxies per sq. arcmin. The mean redshift of the sample is $\langle z_s \rangle \simeq 1.3$. The resultant source redshift distribution is shown in Fig. 3 of More *et al.* [17].

B. Lens galaxy sample

We use the large-scale structure sample compiled as part of the Data Release 11 (DR11)[1] [31] of the SDSS-III BOSS (Baryon Oscillation Spectroscopic Survey) project [32] for measurements of the clustering of galaxies and as lens galaxies for the galaxy-galaxy lensing signal measurements. The lens galaxy sample used in this paper is the same as that used in the first year analysis of HSC data (Sugiyama *et al.* [6] and Miyatake *et al.* [14]). We describe the resultant catalog here briefly.

The BOSS survey is a spectroscopic followup survey of galaxies and quasars selected from the imaging data obtained by the SDSS-I/II, and covers an area of approximately $11,000$ deg^2 [33] using the dedicated 2.5 m SDSS Telescope [34]. Imaging data obtained in five photometric bands (*ugriz*) as part of the SDSS I/II surveys [32,35–40]. were augmented with an additional $3,000$ deg^2 in SDSS DR9 to cover a larger portion of the sky in the southern region [32,38–40]. These data were processed by the SDSS photometric processing pipelines [41–43], and corrected for Galactic extinction [44] to obtain a reliable photometric catalog which serves as an input to select targets for spectroscopy [32]. The resulting spectra were processed by an automated pipeline to perform redshift determination and spectral classification [45]. The BOSS large-scale structure (LSS) samples are selected using algorithms focused on galaxies in different redshifts; $0.15 < z < 0.35$ (LOWZ) and $0.43 < z < 0.7$ (CMASS).

We use three galaxy subsamples in three redshift bins: "LOWZ" galaxies in the redshift range z in $[0.15, 0.35]$ and two subsamples of "CMASS" galaxies, hereafter called "CMASS1" and "CMASS2", respectively, which are obtained by subdividing CMASS galaxies into two redshift bins, $[0.43, 0.55]$ and $[0.55, 0.70]$, respectively. As shown in Fig. 1 of Miyatake *et al.* [5], we define each of the subsamples by selecting galaxies with i-band absolute magnitudes $M_i - 5\log \mathrm{h} < -21.5, -21.9$ and -22.2 for the LOWZ, CMASS1, and CMASS2 samples, respectively. The comoving number densities of these samples for the *Planck* cosmological model [9] are $\bar{n}_g/[10^{-4}(h^{-1}\,\mathrm{Mpc})^{-3}] \simeq 1.8$, 0.74, and 0.45, respectively. These are a few times smaller than the densities of the entire parent LOWZ and CMASS samples. The resultant lens redshift distributions are shown in Fig. 3 of More *et al.* [17].

As described in More *et al.* [17] in detail, as our three clustering observables, we use the projected correlation functions for the three subsamples measured from the entire SDSS DR11 region of about $8,300$ deg^2, and the galaxy-galaxy lensing signal and the cosmic shear correlations measured from the overlap 416 deg^2 area of the HSC-Y3 data. More *et al.* [17] presented the results for various null and systematic tests, which are used to define the scale cuts used in this paper. The covariance matrices for our measurements were computed using a suite of mock catalogs, as described in that paper. We will use these three two-point functions to constrain cosmological parameters.

III. ANALYSIS METHOD

In this section, we describe the theoretical model and the analysis method we use in our cosmological analysis (also see [6,13] for details). We also describe the blinding strategy we adopt for our cosmological analysis and the validation tests of the models/methods as well as the internal consistency tests that we performed before unblinding the results of our analysis.

A. Theoretical model

1. Projected correlation function: $w_p(R)$

To model the projected autocorrelation, w_p, and the galaxy-galaxy lensing signal, $\Delta\Sigma$, which are related to the surrounding matter distribution for the LOWZ, CMASS1, and CMASS2 galaxies, we adopt the "minimal bias" model described in Ref. [13] (also see [6]). This model relates the number density fluctuation field of galaxies to the matter density fluctuation field via a linear galaxy bias parameter, $\delta_g = b_1(z_l)\delta_m$ for each galaxy sample at a representative redshift z_l. Sugiyama *et al.* [13] demonstrated that the minimal bias model can serve as a sufficiently accurate model to recover the cosmological parameters without any significant systematic bias, as long as the model is applied to a sufficiently large scale; $R > 8h^{-1}$ Mpc and $12h^{-1}$ Mpc for w_p and $\Delta\Sigma$, respectively. Given that these conclusions were based on the covariance matrix for HSC Y1 data, we will validate the minimal bias model using mock catalogs of galaxies in Sec. V using the covariance matrix for the HSC-Y3 and SDSS data.

The projected autocorrelation function of galaxies, $w_p(R)$, is related to the three-dimensional real-space correlation function ξ_{gg} such that

$$w_p(R; z_l) = 2 f_{\mathrm{corr}}^{\mathrm{RSD}}(R; z_l) \int_0^{\Pi_{\max}} \mathrm{d}\Pi \xi_{gg}\left(\sqrt{R^2 + \Pi^2}; z_l\right), \tag{2}$$

where $\Pi_{\max}$ is the projection length along the line of sight, and throughout this paper we employ $\Pi_{\max} = 100h^{-1}$ Mpc in the measurement [46]. Typically, the redshift-space distortion (RSD) effects are expected to not contaminate the projected correlation function due to integration along the line-of-sight. But as we model the signal on scales R approaching $\Pi_{\max}$, we account for the residual RSDs

[1] https://www.sdss.org/dr11/.

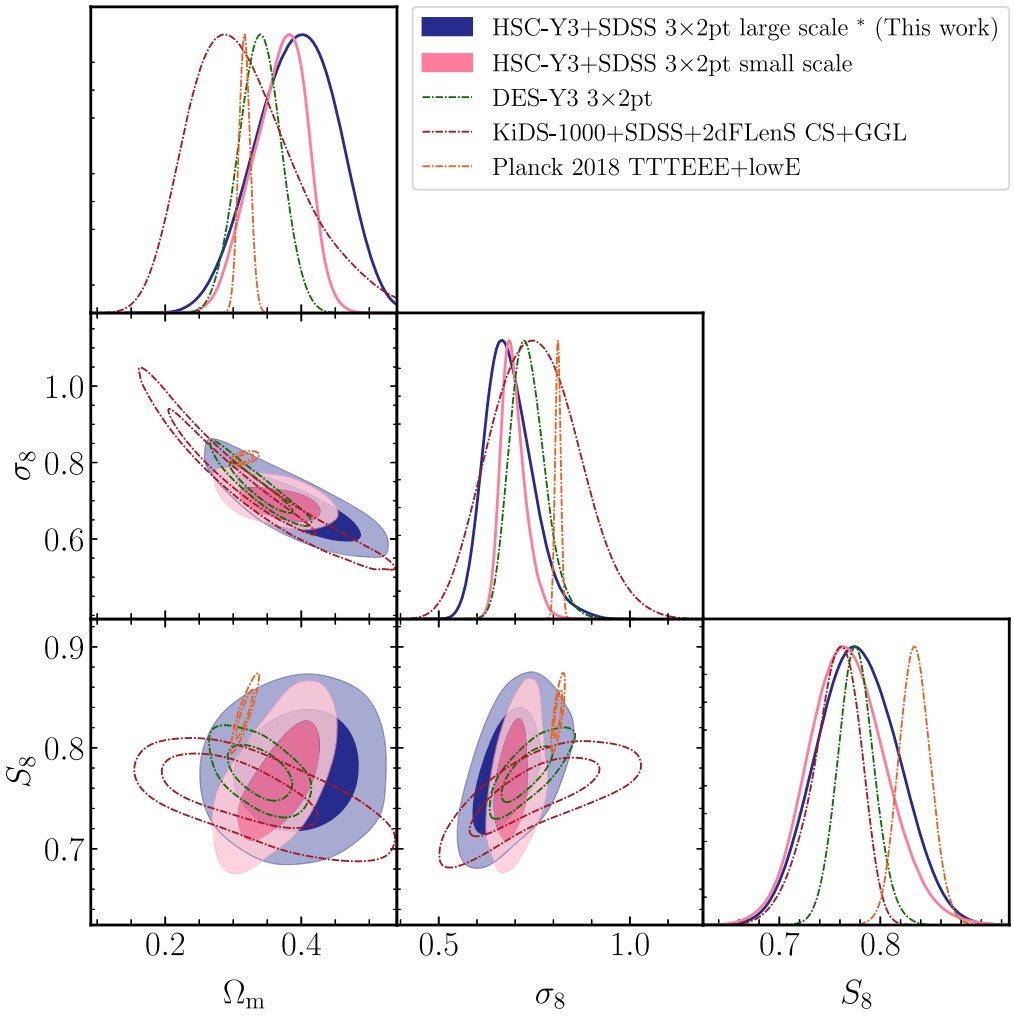

FIG. 1. The cosmological constraint from the HSC Y3 data with the large-scale 3 × 2pt analysis carried out in this work, along with the HSC Y3 small-scale 3 × 2pt analysis in Miyatake *et al.* [16] and external experiments: *Planck* 2018 [9], DES Y3 3 × 2pt [70], and KiDS-1000 [8]. Here the marginal posterior distributions in one- or two-dimensional parameter space are shown for the main cosmological parameters constrained in this work, Ω_m, σ_8, and $S_8 \equiv \sigma_8(\Omega_m/0.3)^{0.5}$.

using the Kaiser RSD factor [11]. This correction factor $f_{\rm corr}^{\rm RSD}(R; z_l)$ depends on the lens redshift and on cosmological parameters, especially Ω_m [see Eq. (48) in Ref. [46] for the definition] [also see [14]]. Using the minimal bias model, we model the three-dimensional, real-space galaxy correlation function as

$$\xi_{gg}(r; z_l) = b_1(z_l)^2 \int_0^\infty \frac{k^2 dk}{(2\pi^2)} P_{mm}^{NL}(k; z_l) j_0(kr), \quad (3)$$

where $j_0(x)$ is the zeroth-order spherical Bessel function, and $b_1(z_l)$ is the linear galaxy bias parameter for each SDSS galaxy sample at the redshift z_l. Throughout this paper, we model the nonlinear matter power spectrum, P_{mm}^{NL}, using `halofit` [47] with the modification suggested by [48] for the assumed cosmological model. While the galaxy clustering signal is also affected by magnification bias, we have checked that its contribution is at the sub-percent level compared to Eq. (2), and hence neglect it in our model.

Each of the lens samples lies in a redshift bin with finite width, and the model signal must be evaluated by averaging the signal within the redshift bin. In this paper, we instead evaluate the model signal at a single representative redshift, defined as the mean redshift of the lens galaxies within each redshift bin. The representative redshift for the LOWZ, CMASS1, and CMASS2 samples are $\bar{z}_l \simeq 0.26$, 0.51, and 0.63, respectively. We have checked that the difference between the signal evaluated at the representative redshift and the signal averaged within the redshift bin is at most 4% of the statistical error in each R bin, as long as we assume the linear galaxy bias does not evolve within the redshift bin.

2. *Galaxy-galaxy weak lensing:* $\Delta\Sigma(R)$

Our model for the galaxy-galaxy lensing signal has two contributions,

$$\Delta\Sigma(R) = \Delta\Sigma_{\rm gG}(R) + \Delta\Sigma_{\rm mag}(R). \quad (4)$$

The first term represents the standard galaxy-galaxy weak-lensing contribution that arises from the average projected matter density distribution around the lens galaxies. Using the minimal bias model we model $\Delta\Sigma_{\rm gG}$ for each of the LOWZ, CMASS1, and LOWZ2 samples as

$$\Delta\Sigma_{\rm gG}(R; z_{\rm l}) = b_1(z_{\rm l})\bar{\rho}_{\rm m0}\int_0^\infty \frac{k{\rm d}k}{2\pi} P_{\rm mm}^{\rm NL}(k; z_{\rm l}) J_2(kR), \quad (5)$$

where $J_2(x)$ is the second-order Bessel function, $\bar{\rho}_{\rm m0}$ is the mean matter density today, and the nonlinear matter power spectrum $P_{\rm mm}^{\rm NL}$ and sample galaxy bias b_1 are the same as in Eq. (3).

The second term on the rhs of Eq. (4) represents magnification bias, which arises from the cross-correlation between the lensing magnification effect in the observed number density field of lens galaxies and the lensing shear on the HSC source galaxy shapes due to the foreground matter density fluctuation along the same line-of-sight direction,

$$\Delta\Sigma_{\rm mag}(R) = \int {\rm d}z_{\rm s} p_{\rm s}(z_{\rm s}) \int {\rm d}z_{\rm l} p_{\rm l}(z_{\rm l}) \widetilde{\Delta\Sigma}_{\rm mag}(R; z_{\rm l}, z_{\rm s}), \quad (6)$$

where $p_{\rm l}(z_{\rm l})$ and $p_{\rm s}(z_{\rm s})$ are the redshift distributions of lens and source galaxies, respectively, that are normalized as $\int {\rm d}z p_i(z) = 1$ ($i = {\rm l}$ or s). For $p_{\rm s}(z_{\rm s})$, we adopt the stacked photo-z posterior distribution of source galaxies as our default choice and will discuss the impact of systematic redshift errors on our cosmology analysis. For $p_{\rm l}(z_{\rm l})$ we can accurately evaluate the distribution using spectroscopic redshifts for lens galaxies. The integrand function, $\widetilde{\Delta\Sigma}_{\rm mag}(R; z_{\rm l}, z_{\rm s})$ is defined as

$$\widetilde{\Delta\Sigma}_{\rm mag}(R; z_{\rm l}, z_{\rm s}) \equiv 2(\alpha_{\rm mag,l} - 1) \times \int_0^\infty \frac{\ell {\rm d}\ell}{2\pi} \Sigma_{\rm c}(z_{\rm l}, z_{\rm s}) C_\kappa(\ell, z_{\rm l}, z_{\rm s}) J_2\left(\ell \frac{R}{\chi_{\rm l}}\right), \quad (7)$$

where $\chi_{\rm l}$ is the comoving distance at the representative redshift $z_{\rm l}$. $\alpha_{\rm mag}$ is a parameter to model the power-law slope of the number counts of the lens galaxies around a magnitude cut in each sample [see Eq. (10) and Fig. 2 in Ref. [5] for the estimated value and error], and $\Sigma_{\rm c}$ is the critical surface density defined as

$$\Sigma_{\rm c}(z_{\rm l}, z_{\rm s}) = \frac{1}{4\pi G} \frac{\chi(z_{\rm s})}{\chi(z_{\rm l})\chi(z_{\rm l}, z_{\rm s})(1 + z_{\rm l})}. \quad (8)$$

Throughout this paper we adopt natural units with $c = 1$ for the speed of light. The angular power spectrum of the lensing convergence field for galaxies at redshifts $z_{\rm l}$ and $z_{\rm s}$ is defined as

$$C_\kappa(\ell; z_{\rm l}, z_{\rm s}) = \int {\rm d}\chi \frac{W(\chi, \chi_{\rm l}) W(\chi, \chi_{\rm s})}{\chi^2} P_{\rm mm}^{\rm NL}\left(\frac{l + 1/2}{\chi}; z\right), \quad (9)$$

where the lensing efficiency kernel is defined using $\chi_s = \chi(z_{\rm s})$ as

$$W(\chi, \chi_s) \equiv \frac{3}{2}\Omega_{\rm m} H_0^2 (1 + z) \frac{\chi(\chi_{\rm s} - \chi)}{\chi_{\rm s}}. \quad (10)$$

3. Cosmic shear correlation functions: $\xi_\pm$

We model the two-point correlation functions of source galaxy shapes as a sum of the following three terms

$$\xi_\pm(\vartheta) = \xi_{\rm GG,\pm}(\vartheta) + \xi_{\rm GI,\pm}(\vartheta) + \xi_{\rm II,\pm}(\vartheta). \quad (11)$$

The first term is the "gravitational-gravitational" term (i.e., cosmic shear, "GG"), the second term is the "gravitational-intrinsic" correlation ("GI") [49] that arises in pairs of galaxies for which some common large-scale structure along the line of sight affects the intrinsic shapes of one of the galaxies and results in a gravitational lensing shear on the other, while the third term is the "intrinsic-intrinsic" ("II") IA contribution [50].

The GG term of Eq. (11) is defined in terms of the cosmic shear power spectrum as

$$\xi_{\rm GG,\pm}(\vartheta) = \int \frac{\ell {\rm d}\ell}{2\pi} C_\kappa(\ell) J_{0/4}(\ell\vartheta), \quad (12)$$

where the zeroth- and fourth-order Bessel functions are for $\xi+$ and ξ_-, respectively. C_κ is the angular power spectrum of the lensing convergence, defined as

$$C_\kappa(\ell) = \int {\rm d}\chi \frac{q^2(\chi)}{\chi^2} P_{\rm mm}^{\rm NL}\left(\frac{\ell + 1/2}{\chi}; z\right), \quad (13)$$

where $q(\chi)$ is the lensing efficiency kernel averaged over the source redshift distribution defined as

$$q(\chi) = \int {\rm d}z_{\rm s} p_s(z_{\rm s}) W(\chi, \chi_s). \quad (14)$$

In this paper, we use a single source sample, and hence we have no tomographic cosmic shear signals.

To model the GI and II terms of Eq. (11), we employ the nonlinear alignment model (NLA) [51],

$$C_{\rm GI}(\ell) = 2\int {\rm d}\chi \frac{F(\chi) H(z) p_{\rm s}(z) q(\chi)}{\chi^2} P_{\rm mm}^{\rm NL}\left(\frac{\ell + 1/2}{\chi}; z\right), \quad (15)$$

$$C_{\rm II}(\ell) = \int {\rm d}\chi \left[\frac{F(\chi)H(z)p_{\rm s}(z)}{\chi}\right]^2 P_{\rm mm}^{\rm NL}\left(\frac{\ell+1/2}{\chi}; z\right). \tag{16}$$

Here following the conventional method in the literature e.g., [3], we introduced the redshift- and cosmology-dependent factor $F(\chi)$ that relates the intrinsic galaxy ellipticity and the gravitational tidal field and is parametrized as

$$F(\chi) = -A_{\rm IA}C_1\rho_{\rm c}\frac{\Omega_{\rm m}}{D_+(z)}, \tag{17}$$

where $A_{\rm IA}$ is a free parameter that describes the amplitude of the NLA model, $C_1 = 5\times10^{-14}h^{-2}{\rm M}_\odot^{-1}$ Mpc^3 is a normalization constant, $\rho_{\rm c}$ is the critical mass density at $z=0$, and $D_+(z)$ is the linear growth factor normalized to unity at $z=0$. Since we use the cosmic shear correlations for a single sample of the source galaxies, i.e., no lensing tomography, we employ a single parameter $A_{\rm IA}$ to model the IA contamination, and do not include a parameter to model the redshift dependence of the IA effect.

B. Modeling residual systematic errors

In this section, we present a method to model possible residual systematic effects in the measured signals. In our method, we include these effects in the model predictions rather than in the measured signals to keep the data vector and the covariance invariant.

1. Residual systematic redshift uncertainty: $\Delta z_{\rm ph}$

Residual systematic error in the mean redshift of the HSC source galaxies is one of the most important systematic effects in weak-lensing measurements, i.e., $\Delta\Sigma$ and $\xi_\pm(\vartheta)$ in our data vector. To study the impact of residual redshift error, we introduce a nuisance parameter to model the systematic error in the mean source redshift by shifting the posterior distribution of source redshifts, given as $z^{\rm est} = z^{\rm true} + \Delta z_{\rm ph}$ [5,52,53]. Please see Sec. IIIA2 in Miyatake *et al.* [16] and Zhang *et al.* [54] for a justification of our parametrization ($\Delta z_{\rm ph}$) to model the impact of residual source redshift uncertainty on the weak-lensing observables. Therefore, we use the shifted $P(z)$ distribution to model the mean of the true redshift distribution as

$$p_{\rm s}^{\rm true}(z) = p_{\rm s}^{\rm est}(z+\Delta z_{\rm ph}). \tag{18}$$

Thus, if $\Delta z_{\rm ph} > 0$ or < 0, the true mean redshift of our sources becomes lower or higher than what is anticipated from the photo-z estimates, respectively.

For $\Delta\Sigma$ (Eq. (4), we first need to recompute the average lensing efficiency $\langle\Sigma_{\rm cr}^{-1}\rangle$ and the weight $w_{\rm ls}$ using the shifted redshift distribution: we define the correction factor as

$$f_{\Delta\Sigma}(\Delta z_{\rm ph}) \equiv \frac{\sum_{\rm ls} w_{\rm ls}\langle\Sigma_{\rm c}^{-1}\rangle_{\rm ls}^{\rm true}/\langle\Sigma_{\rm c}^{-1}\rangle_{\rm ls}^{\rm est}}{\sum_{\rm ls} w_{\rm ls}}, \tag{19}$$

where the weight is given as $w_{\rm ls} = w_{\rm l}w_{\rm s}\langle\Sigma_{\rm c}^{-1}\rangle_{\rm ls}^2$ and $w_{\rm l}$ and $w_{\rm s}$ are weights given in the HSC shape catalog and the BOSS catalog, respectively [see Sec. IIB in Ref. [5] for the definitions]. We compute the correction factor for each of the three lens samples, LOWZ, CMASS1, and CMASS2. In our method, we multiply the correction factor by the model template of $\Delta\Sigma$ as

$$\Delta\Sigma^{\rm corr}(R; z_{\rm l}, \Delta z_{\rm ph}) = f_{\Delta\Sigma}(\Delta z_{\rm ph}; z_{\rm l})\Delta\Sigma(R|z_{\rm l}). \tag{20}$$

Note that $\Delta\Sigma$ includes both the galaxy-galaxy weak lensing and the magnification term in Eq. (4); $\Delta\Sigma = \Delta\Sigma_{\rm gG} + \Delta\Sigma_{\rm mag}$, and we also use the shifted redshift distribution of source galaxies to compute the magnification term, $\Delta\Sigma_{\rm mag}$.[2]

Similarly, for nonzero $\Delta z_{\rm ph}$, we recompute the model prediction for the cosmic shear correlation functions $\xi_\pm(\vartheta)$ using the shifted redshift distribution of the source galaxies.

2. Correction for the reference cosmology used in our measurement

In the measurements of $w_{\rm p}$ and $\Delta\Sigma$, we need to assume a "reference" cosmology to convert the angular separation between galaxies in the pair to the projected separation R, and the redshift difference to the radial separation, Π. For $\Delta\Sigma$, we also need the reference cosmology to compute $\langle\Sigma_{\rm c}\rangle^{-1}$, which is needed to convert the shear to $\Delta\Sigma$. In More *et al.* [17], where we present the measurements, we assume a reference cosmology with $\Omega_{\rm m}^{\rm ref} = 0.279$, which is only the relevant parameter for a flat ΛCDM model. However, the reference cosmology generally differs from the underlying true cosmology, and we need to correct for the discrepancy in our cosmological parameter analysis. We follow Ref. [55] in order to perform these corrections. We denote the cosmological parameters in the parameter inference as $\mathbb{C}$ and the reference cosmological parameters for the measurements as $\mathbb{C}^{\rm ref}$. Similarly to Sec. III B 1, we can derive the correction factors, by keeping the observables invariant. The corrections for R and Π are obtained as follows:

$$\begin{aligned} R &= \frac{\chi(z_{\rm l};\mathbb{C})}{\chi(z_{\rm l};\mathbb{C}^{\rm ref})}R^{\rm ref}, \\ \Pi &= \frac{E(z_{\rm l};\mathbb{C}^{\rm ref})}{E(z_{\rm l};\mathbb{C})}\Pi^{\rm ref}, \end{aligned} \tag{21}$$

Here $E(z) \equiv H(z)/H_0$. Thus, we include the measurement corrections in the theoretical templates of $\Delta\Sigma$ and $w_{\rm p}$ as

[2]Note that the definition of $f_{\Delta\Sigma}$ is the inverse of the similar correction factor $f_{\rm ph}$ used in the HSC-Y1 papers [5,6].

$$\Delta\Sigma^{\rm ref}(R^{\rm ref},z_{\rm l}|\mathbb{C},\Delta z_{\rm ph})=f_{\Delta\Sigma}(z_{\rm l}|\mathbb{C},\Delta z_{\rm ph})\Delta\Sigma(R,z_{\rm l}|\mathbb{C}),$$
$$w_{\rm p}(R^{\rm ref},z_{\rm l}|\mathbb{C})=2f_{\rm corr}^{\rm RSD}(R,z_{\rm l};\mathbb{C})\frac{E(z_{\rm l};\mathbb{C})}{E(z_{\rm l};\mathbb{C}^{\rm ref})}\times\int_0^{\Pi_{\rm max}}{\rm d}\Pi\xi_{\rm gg}\left(\sqrt{R^2+\Pi^2},z_{\rm l};\mathbb{C}\right),\quad(22)$$

where R and Π are given in terms of $R^{\rm ref}$ and $\Pi^{\rm ref}$ via the above Eq. (21) and evaluated at the sampling points of $R^{\rm ref}$ and $\Pi^{\rm ref}$ used in the measurements. Note that we adopt $\Pi_{\rm max}=[E(\mathbb{C}^{\rm fid})/E(\mathbb{C})]\Pi_{\rm max}^{\rm ref}=[E(\mathbb{C}^{\rm ref})/E(\mathbb{C})]\times 100h^{-1}$ Mpc, as we use the fixed $\Pi_{\rm max}^{\rm fid}=100h^{-1}$ Mpc in the measurement. The overall correction factor for $\Delta\Sigma$ is defined as

$$f_{\Delta\Sigma}(z_{\rm l}|\mathbb{C},\Delta z_{\rm ph})\equiv\frac{\sum_{\rm ls}w_{\rm ls}\langle\Sigma_{\rm c}^{-1}\rangle_{\rm ls}^{\rm true,\mathbb{C}}/\langle\Sigma_{\rm c}^{-1}\rangle_{\rm ls}^{\rm est,\mathbb{C}^{\rm ref}}}{\sum_{\rm ls}w_{\rm ls}}.\quad(23)$$

Now this correction factor accounts for both the effects of residual photo-z errors ($\Delta z_{\rm ph}$) and the use of the reference cosmology.

Note that the theoretical templates of $\xi_\pm(\vartheta)$ for cosmic shear correlation functions are not affected by the varying cosmological models, as $\xi_\pm$ is given as a function of the observed angular separation ϑ.

3. Residual-multiplicative shear bias

We account for possible residual biases on the weak-lensing shear calibration, with a nuisance parameter describing the residual multiplicative bias Δm,

$$\Delta\Sigma(R;\Delta m)=(1+\Delta m)\Delta\Sigma(R;\Delta m=0),\quad(24)$$

$$\xi_\pm(\vartheta;\Delta m)=(1+\Delta m)^2\xi_\pm(\vartheta;\Delta m=0).\quad(25)$$

Since we use the same source sample for both the galaxy-galaxy lensing and the cosmic shear measurements, we use the same residual multiplicative bias parameter for $\Delta\Sigma$ and $\xi_\pm$.

4. Residual PSF modeling errors

Systematic tests of the HSC-Y3 shear catalog presented in Li *et al.* [26] indicate that there are small residual correlations between galaxy ellipticities and PSF ellipticities resulting from imperfect PSF correction. Such residual correlations could produce artificial galaxy shape-shape correlations and hence bias the cosmic shear measurements. Here we examine the impact of these systematics in our cosmic shear measurements, assuming that the measured galaxy shapes have an additional additive bias given by

$$\epsilon^{\rm (sys)}=\alpha_{\rm psf}\epsilon^{\rm p}+\beta_{\rm psf}\epsilon^{\rm q}.\quad(26)$$

The first term, referred to as PSF leakage, represents the systematic error proportional to the PSF model ellipticity $\epsilon^{\rm p}$ due to the imperfection in the method used to correct the galaxy shapes for the impact of the PSF. The second term represents the systematic error associated with the difference between the model PSF ellipticity, $\epsilon^{\rm p}$, and the true PSF ellipticity. This difference is estimated from individual "reserved" stars $\epsilon^{\rm star}$, i.e., $\epsilon^{\rm q}\equiv\epsilon^{\rm p}-\epsilon^{\rm star}$ [56]. A coherent residual PSF ellipticity $e^{\rm q}$ indicates an imperfect PSF estimate, which should propagate to shear estimates of galaxies.

When the observed galaxy ellipticity is contaminated by $\epsilon^{\rm (sys)}$, these systematic terms cause an additional contamination to the measured cosmic shear correlation functions as

$$\xi_{\rm psf,\pm}(\vartheta)=\alpha_{\rm psf}^2\hat{\xi}_\pm^{\rm pp}(\vartheta)+2\alpha_{\rm psf}\beta_{\rm psf}\hat{\xi}_\pm^{\rm pq}(\vartheta)+\beta_{\rm psf}^2\hat{\xi}_\pm^{\rm qq}(\vartheta),\quad(27)$$

where $\hat{\xi}_\pm^{\rm pp}$, $\hat{\xi}_\pm^{\rm qq}$ and $\hat{\xi}_\pm^{\rm pq}$ represent the autocorrelation of the model PSF ellipticity $\epsilon_\pm^{\rm p}$, the autocorrelation of the residual PSF ellipticity $\epsilon_\pm^{\rm q}$, and the cross-correlation of $\epsilon_\pm^{\rm p}$ and $\epsilon_\pm^{\rm q}$, respectively. The hat notation, "$\hat{}$", denotes the correlation function measured from the HSC data using the model PSF and the reserved stars (see More *et al.* [17]). The proportional coefficients $\alpha_{\rm psf}$ and $\beta_{\rm psf}$ are estimated by cross-correlating $\epsilon_\pm^{\rm p}$ and $\epsilon_\pm^{\rm q}$ with the observed galaxy ellipticities as

$$\hat{\xi}_\pm^{\rm gp}(\vartheta)=\alpha_{\rm psf}\hat{\xi}_\pm^{\rm pp}(\vartheta)+\beta_{\rm psf}\hat{\xi}_\pm^{\rm pq}(\vartheta),$$
$$\hat{\xi}_\pm^{\rm gq}(\vartheta)=\alpha_{\rm psf}\hat{\xi}_\pm^{\rm pq}(\vartheta)+\beta_{\rm psf}\hat{\xi}_\pm^{\rm qq}(\vartheta),\quad(28)$$

where $\hat{\xi}_\pm^{\rm gp}$ and $\hat{\xi}_\pm^{\rm gq}$ are the measured cross-correlations between galaxy ellipticities, used for the cosmic shear data vector, and $\epsilon_\pm^{\rm p}$ and $\epsilon_\pm^{\rm q}$. As shown in More *et al.* [17], we found $\alpha_{\rm psf}=-0.0292\pm0.0129$ and $\beta_{\rm psf}=-2.59\pm1.65$ for our fiducial source sample.

To take into account the impact of these additive shear residuals on parameter inference, we add the contamination term $\xi_{\rm psf,\pm}$ [Eq. (27)] to the model cosmic shear correlation function $\xi_\pm$ in Eq. (11) and then estimate parameters by varying the parameters $\alpha_{\rm psf}$ and $\beta_{\rm psf}$ with the Gaussian priors with widths inferred from the above errors. Note that the above PSF systematics causes additive shear bias, and does not cause a bias in the galaxy-galaxy weak lensing [57].

We note that the PSF systematics model we adopted here is based on the second moments of PSF as done in Hamana *et al.* [4], while the HSC-Y3 tomographic cosmic shear analyses [18,19] use a PSF systematics model with additional terms including the fourth moments [54]. Because the contamination from PSF systematics effects in the cosmic shear signal is relatively small for high-redshift HSC source galaxies compared to the signal at lower redshift, the second-moment-based PSF systematics model

is sufficient for our analysis. We explicitly validate the use of our PSF systematics model in Appendix A by performing the cosmological parameter analysis on a synthetic data vector including the measured PSF systematics up to the fourth-moments in the synthetic cosmic shear data vector.

C. Summary: Theoretical template

For the convenience of the following discussion, here we summarize the theoretical templates, explicitly showing which parameters are used to model each of the theoretical templates,

$$\begin{aligned}\Delta\Sigma^{\rm t}(R^{\rm ref}, z_{\rm l}|\mathbb{C}, b_1(z_{\rm l}), \Delta z_{\rm ph}, \Delta m, \alpha_{\rm mag}(z_{\rm l})) &= (1+\Delta m)\Delta\Sigma^{\rm ref}(R^{\rm ref}, z_{\rm l}|\mathbb{C}, b_1(z_{\rm l}), \Delta z_{\rm ph}, \alpha_{\rm mag}(z_{\rm l})),\\ &\quad\times w_{\rm p}^{\rm t}(R^{\rm ref}, z_{\rm l}|\mathbb{C}, b_1(z_{\rm l})):\ \text{Eqs. (2) and (22)},\\ \xi_{\pm}^{\rm t}(\vartheta|\mathbb{C}, \Delta z_{\rm ph}, A_{\rm IA}, \Delta m, \alpha_{\rm psf}, \beta_{\rm psf}) &= (1+\Delta m)^2\xi_{\pm}(\vartheta|\mathbb{C}, \Delta z_{\rm ph}, A_{\rm IA}) + \xi_{\pm,{\rm psf}}(\vartheta|\alpha_{\rm psf}, \beta_{\rm psf}).\end{aligned} \tag{29}$$

For $\Delta\Sigma^{\rm ref}$ and $w_{\rm p}^{\rm t}$, we compute these model predictions at the sampling points of $R^{\rm ref}$ for each of the LOWZ, CMASS1, and CMASS2 samples at their representative redshift. Here $\mathbb{C}$ denotes a cosmological model sampled in parameter inference, and characterized by five cosmological parameters for the flat ΛCDM model, $(\Omega_{\rm de}, \ln(10^{10}A_{\rm s}), \omega_{\rm c}, \omega_{\rm b}, n_{\rm s})$. $b_1(z_{\rm l})$ denotes the linear bias parameter for the LOWZ, CMASS1, or CMASS2 sample, and other parameters are nuisance parameters to model the residual systematic errors in photo-z's, magnification bias, multiplicative shear bias, PSF modeling, and intrinsic alignment. For our baseline analysis, we have 16 parameters in total; $16 = 5(\mathbb{C}) + 3\times 1(b_1) + 8(\text{nuisance})$.

D. Bayesian inference: Likelihood and prior

To infer parameters $\boldsymbol{\theta}$ from the measured clustering observables, we compare a "data vector", denoted as $\hat{\boldsymbol{d}}$, to a "theoretical model template", denoted as $\boldsymbol{t}$. We define the data vector from the measured signals of $w_{\rm p}$, $\Delta\Sigma$, and $\xi_{\pm}$ as

$$\boldsymbol{d} \equiv \{\hat{w}_{\rm p}(R_i^{\rm ref}|z_{\rm l}), \widehat{\Delta\Sigma}(R_j^{\rm ref}|z_{\rm l}), \hat{\xi}_{\pm}(\vartheta_k)\}, \tag{30}$$

where $z_{\rm l}$ stands for the representative redshift of either LOWZ, CMASS1, or CMASS2 sample. Here we emphasize that the measured signals are sampled at discrete values of of separation, $R_i^{\rm ref}$, $R_j^{\rm ref}$, and ϑ_k for $\hat{w}_{\rm p}$, $\widehat{\Delta\Sigma}$ and $\hat{\xi}_{\pm}$, respectively, where $R_i^{\rm ref}$ and $R_j^{\rm ref}$ are estimated from the observed angular separations between galaxies in the pair assuming the reference cosmology as we described above.

For $w_{\rm p}$, we use the signals in the range of $R^{\rm ref} = [8, 80]h^{-1}$ Mpc. The minimum scale cut is determined so that the minimum bias model fairly well describes the signals [6,13], without being so affected by the strongly nonlinear clustering. The maximum scale cut is determined such that our constraint purely comes from the large scale clustering amplitude, and does not include information from the baryonic acoustic oscillations. The constraining power of cosmological parameters is mainly from scales around the minimum scale cut, where have higher signal-to-noise ratios. We take 14 logarithmically-spaced bins for each of the LOWZ, CMASS1, and CMASS2 samples. For $\Delta\Sigma$, we use the signals in the range of $R^{\rm ref} = [12, 30]$, $[12,\ 40]$ or $[12, 80]h^{-1}$ Mpc for the LOWZ, CMASS1, or CMASS2 sample, respectively. The minimum scale cuts are determined by the same reason as the $w_{\rm p}$ case, while the maximum scale cuts are determined based on the systematic tests, i.e., where we do not find any significant signal of nonlensing $\Delta\Sigma_{\times}$ at scales below the maximum cuts compared to the statistical errors. The scale cuts give 4, 5, and 8 logarithmically-spaced radial bins for the LOWZ, CMASS1, and CMASS2 samples, respectively. For cosmic shear we use 8 angular separation bins in the range of $\vartheta = [7.9, 50.1]$ arcmin for $\xi_+(\vartheta)$, while seven angular bins in $\vartheta = [31.6, 158]$ arcmin for $\xi_-(\vartheta)$. Thus we use 74 data points in total: $42(=3\times 14)$ for $w_{\rm p}$, $17(=4+5+8)$ for $\Delta\Sigma$ and $15(=7+8)$ for $\xi_{\pm}$, respectively.

For the theoretical template $\boldsymbol{t}$, we construct the "model vector" of the clustering correlation functions computed using a set of model parameters $\boldsymbol{\theta}$ within the flat ΛCDM framework,

$$\boldsymbol{t}(\boldsymbol{\theta}) \equiv \{w_{\rm p}^{\rm t}(R_i^{\rm ref}, z_{\rm l}|\boldsymbol{\theta}), \Delta\Sigma^{\rm t}(R_j^{\rm ref} z_{\rm l}|\boldsymbol{\theta}), \xi_{\pm}^{\rm t}(\vartheta_k|\boldsymbol{\theta})\}, \tag{31}$$

where the theoretical templates of clustering observables (denoted by the superscript "t") are computed at the representative redshift of each lens sample, $z_{\rm l}$, using Eq. (29). We use the publicly-available `FFTLog` code developed in Ref. [58], which is a modified version from the original code [59], to perform Hankel transforms in the model-prediction calculations. We also use `FFTlog` to compute the average of model prediction within a finite radial bin width used in the measurements; $\Delta\ln R = 0.169$ for $w_{\rm p}$, $\Delta\ln R = 0.246$ for $\Delta\Sigma$ and $\Delta\ln\vartheta = 0.242$ for $\xi_{\pm}$.

We assume that the likelihood of the data vector compared to the model vector follows a multivariate Gaussian distribution:

$$\ln \mathcal{L}(\boldsymbol{d}|\boldsymbol{\theta}) = -\frac{1}{2}[\boldsymbol{d}-\boldsymbol{t}(\boldsymbol{\theta})]^T \boldsymbol{C}^{-1}[\boldsymbol{d}-\boldsymbol{t}(\boldsymbol{\theta})], \quad (32)$$

where $\boldsymbol{C}$ is the covariance matrix of data vector (see More *et al.* [17] for details), $\boldsymbol{C}^{-1}$ is the inverse matrix. The covariance matrix is estimated in [17] from $1404(=108\times13)$ realizations of the mock signals [60,61]. When we compute the inverse covariance in the likelihood, we multiply the factor $(108\times13-74-2)/(108\times13-1)=0.95$ to obtain the inverse covariance [62].[3] The cross covariance between galaxy-galaxy lensing and cosmic shear is included because we use the same mock catalogs for clustering, galaxy-galaxy lensing, and cosmic shear measurements. Since the overlapping region between the HSC-Y3 and SDSS DR11 survey footprints, which has about 416 deg^2, is much smaller than the SDSS DR11 area (about $8,300$ deg^2), we ignore the cross-covariance between the clustering ($w_{\rm p}$) and galaxy-galaxy lensing ($\Delta\Sigma$). The mock catalogs used in the covariance matrix estimation are generated using full-sky simulations [63], and hence the covariance automatically includes the super-sample covariance contribution [64]. The additional covariance contribution due to the magnification bias effect on the lens galaxy distribution is analytically estimated and added onto the estimate from mock measurements [6]. See More *et al.* [17] for more detail of the covariance matrix estimation.

We construct a posterior probability distribution for the parameters $\boldsymbol{\theta}$ given the data vector $\boldsymbol{d}$, denoted as $\mathcal{P}(\boldsymbol{\theta}|\boldsymbol{d})$, by performing Bayesian inference,

$$\mathcal{P}(\boldsymbol{\theta}|\boldsymbol{d}) \propto \mathcal{L}(\boldsymbol{d}|\boldsymbol{\theta})\Pi(\boldsymbol{\theta}), \quad (33)$$

where $\Pi(\boldsymbol{\theta})$ is the prior distribution of $\boldsymbol{\theta}$.

In Table I, we summarize the model parameters and their priors. The first section summarizes the cosmological parameters; $\Omega_{\rm m}(=1-\Omega_{\rm de})$ and $\ln 10^{10}A_{\rm s}$ are the parameters to which our weak-lensing and clustering observables are most sensitive, and we adopt uninformative uniform priors on these model parameters. On the other hand, the weak-lensing and clustering analyses are not sensitive to $\omega_b=\Omega_{\rm b}h^2$ and $n_{\rm s}$, and hence we adopt informative priors using normal distributions; we use a BBN prior for ω_b [65–67], and a Planck prior on $n_{\rm s}$ [9]. Note that we increased the uncertainty of the Planck prior on $n_{\rm s}$ by a factor of three to be conservative. The parameters $b_1(z_{\rm i})$ in the second section are the linear galaxy bias parameters for $i=$ LOWZ, CMASS1, and CMASS2. We use uninformative priors on each of these parameters, given that our samples could be affected by assembly bias [13].

[3]We mistakenly omitted one realization of the full sky simulation for the covariance estimation. Thus, in practice, we use $(107\times13-74-2)/(107\times13-1)=0.946$ for the Hartlap factor instead.

TABLE I. Model parameters and priors used in our cosmological parameter inference. The label $\mathcal{U}(a,b)$ denotes a uniform (or equivalently flat) distribution with minimum a and maximum b, while $\mathcal{N}(\mu,\sigma)$ denotes a normal distribution with mean μ and width σ. For the residual photo-z error parameter, $\Delta z_{\rm ph}$, we employ the informative Gaussian prior $\mathcal{N}(-0.05,0.09)$ in our baseline analysis, which is taken from the companion analysis result in Miyatake *et al.* [16] that perform a parameter inference by comparing the halo model based predictions to exactly the same clustering observables (down to the smaller scale cuts for $\Delta\Sigma$ and $w_{\rm p}$).

Parameter	Prior
Cosmological parameters	
$\Omega_{\rm de}$	$\mathcal{U}(0.4594,0.9094)$
$\ln(10^{10}A_{\rm s})$	$\mathcal{U}(1.0,5.0)$
$\omega_{\rm c}$	$\mathcal{U}(0.0998,0.1398)$
$\omega_{\rm b}$	$\mathcal{N}(0.02268,0.00038)$
$n_{\rm s}$	$\mathcal{N}(0.9649,3\times0.0042)$
Galaxy bias parameters	
$b_1(z_{\rm LOWZ})$	$\mathcal{U}(0.1,5.0)$
$b_1(z_{\rm CMASS1})$	$\mathcal{U}(0.1,5.0)$
$b_1(z_{\rm CMASS2})$	$\mathcal{U}(0.1,5.0)$
Magnification bias parameters	
$\alpha_{\rm mag}(z_{\rm LOWZ})$	$\mathcal{N}(2.259,0.5)$
$\alpha_{\rm mag}(z_{\rm CMASS1})$	$\mathcal{N}(3.563,0.5)$
$\alpha_{\rm mag}(z_{\rm CMASS2})$	$\mathcal{N}(3.729,0.5)$
Photo-z / Shear errors	
$\Delta z_{\rm ph}$	$\mathcal{N}(-0.05,0.09)$
Δm	$\mathcal{N}(0.0,0.01)$
PSF residuals	
$\alpha_{\rm psf}$	$\mathcal{N}(-0.026,0.010)$
$\beta_{\rm psf}$	$\mathcal{N}(-1.656,1.326)$
Intrinsic alignment parameters	
$A_{\rm IA}$	$\mathcal{U}(-5,5)$

For the magnification bias parameter, $\alpha_{\rm mag}(z_{\rm l})$, we adopt a prior using a normal distribution; the central value is taken from the estimated slope of number counts at luminosity cut, while we adopt a relatively wide width, $\sigma(\alpha_{\rm mag})=0.5$, for a conservative analysis.

The fourth section summarizes the residual redshift and the residual multiplicative bias parameters. In the small-scale analysis by Miyatake *et al.* [16], we find that the weak-lensing signals have a statistical power to calibrate the residual redshift error parameter ($\Delta z_{\rm ph}$) to the precision of $\sigma(\Delta z_{\rm ph})\simeq0.1$, based on the method in Ref. [53]. On the other hand, as discussed in Sec. VI, we find that the statistical power of the large-scale signals is not sufficient to calibrate $\Delta z_{\rm ph}$. Therefore, in this paper, we use a Gaussian prior on $\Delta z_{\rm ph}$, $\mathcal{N}(-0.05,0.09)$, that is inferred from the mode and the credible interval of the posterior distribution of $\Delta z_{\rm ph}$ in the fiducial small-scale analysis by

the companion work Miyatake *et al.* [16]. That is, we employ the prior that is centered at $\Delta z_{\rm ph} = -0.05$, meaning that the source redshift distribution inferred from the photo-z estimates is lower than the true distribution by $|\Delta z_{\rm ph}| = 0.05$.

For the prior on the multiplicative shear bias, we use the Gaussian prior with zero mean and width of $\sigma = 0.01$, which is estimated from HSC galaxy image simulations [26]. The fifth section summarizes the PSF residual systematics modeling parameters. We use Gaussian prior for these model parameters. The center and width are estimated from the cross-correlation between star shapes and galaxy shapes (see [17] for more detail). The sixth section summarizes the single intrinsic alignment parameter of the NLA model for this source sample, for which we use an uninformative uniform prior. The dimension of the fiducial model parameter vector is 16 in total, 5 for the cosmological parameters and 11 for the nuisance parameters.

We sample parameters from their posterior distribution given the data vector using the Monte Carlo method in this high-dimensional parameter space. In particular, we utilize the nested sampling algorithm implemented in `MultiNest` [68] from the python interface `PyMultiNest` [69]. `MultiNest` has two hyperparameters, the live points `nlive` and the sampling efficiency rate `efr`. We use `nlive` $= 600$ and `efr` $= 0.3$ as the fiducial setup. Another hyperparameter, the tolerance `tol`, is set to 0.1, and replaced with a smaller value if necessary to check for convergence.

In this paper, we report the inference result in the format of

$$\text{mode}^{+34\%\ \text{upper}}_{-34\%\ \text{lower}}(\text{MAP}), \tag{34}$$

where the mode is the peak value of a parameter in the one-dimensional marginal posterior distribution, the 68% credible interval is defined as the highest density interval of the posterior, and "+34% upper" and "−34% lower" are the upper and lower limit of the 68% credible interval (see Fig. 3 of [6] for the illustration of the definitions of these statistics of marginalized posterior). We also report the "MAP" value of the parameter that is the parameter value at the maximum *a posteriori* model which has the highest posterior value in the chain. The mode value is defined with the marginal posterior and thus subject to the projection effect of the posterior distribution from the full-parameter space, while the MAP is not. Thus, a significant difference between the mode and MAP value may indicate the degree to which the mode value is affected due to lower-dimensional projection of the posterior distribution. However, we should note that the estimation of the MAP value can be noisy due to a finite number of samples in the chain, especially in the presence of severe parameter degeneracy(degeneracies), resulting in a MAP that corresponds to a local minimum in the posterior surface. Therefore, we will use the MAP value and its difference from the mode as an indicator of projection effects. In the summary table that gives the cosmological constraints for various setups and tests, we also report the mean value as the third point estimate so that one can easily compare our results with external results that also use the mean.

IV. BLINDING SCHEME AND INTERNAL CONSISTENCY

To avoid confirmation bias, we perform our cosmological analysis in a blind fashion. The details of the blinding scheme can be also found in Sec. IIB of More *et al.* [17]. We employ a two-tier blinding strategy to avoid unintentional unblinding during the cosmological analysis. The two tiers are as follows:

(i) *Catalog level*: The analysis team performs the cosmological analysis using three different weak-lensing shape catalogs. Only one is the true catalog and the other two catalogs have multiplicative biases which are different from the truth (see below for details). The analysis team members do not know which is the true catalog.

(ii) *Analysis level*: When the analysis team makes plots comparing the measurements with theoretical models, the y-axis values (e.g., the amplitudes of $\Delta\Sigma$) are hidden and the analysis team is not allowed to see the values of cosmological parameters used in the theoretical models. When the analysis team makes plots showing the credible intervals of cosmological parameters (i.e., the posterior distribution), the central value(s) of parameter(s) are shifted to zero, and only the range of the credible interval(s) can be seen. Finally, the analysis team does not compare the posterior for cosmological parameter(s) or the model predictions with external results such as the *Planck* CMB cosmological parameters prior to unblinding.

See Sec. IIB of More *et al.* [17] (see also [18]) for details of how the blinded catalogs were constructed in a manner that prevents accidental unblinding by the analysis team. The use of these catalogs means that the analysis team must perform three analyses, but this method avoids the need for reanalysis once the catalogs are unblinded.

The set of the three shape catalogs used in this paper is shared with the two companion papers, More *et al.* [17] presenting details of the measurements of observables used in this paper and Miyatake *et al.* [16] presenting the cosmological parameter estimation from the same signals as those of this paper, but including the information down to smaller scales and using the halo model-based method. We imposed the following criteria for deciding to unblind our results:

(i) Analysis software is made available to collaboration members and specific members have reviewed each part of the code.

(ii) Validation tests of the cosmology analysis pipeline are performed using synthetic data vectors, some of which are generated using mock catalogs of galaxies. In particular, the key cosmological parameter S_8 must be recovered to within 0.5σ (σ is the marginalized credible interval), for the fiducial mock catalogs (see below).

(iii) Internal consistency tests are performed to check whether the estimate of the key cosmological parameter is changed, compared to the fiducial analysis method, using subsets of data vector and/or different analysis setups. Table II summarizes the internal consistency tests that we performed before unblinding.

(iv) The goodness of fit of the best-fit model predictions to the data vector in each of the three blind catalogs is quantified.

The analysis team resolved that the results would be published regardless of the outcome once the results are unblinded, without any changes or modifications to the

TABLE II. Internal consistency tests carried out for the cosmological parameter analysis. All of the analyses are performed before unblinding the results. In this paper, we use the prior $\Pi(\Delta z_{\rm ph}) = \mathcal{N}(-0.05, 0.09)$, which is obtained from the small-scale 3×2pt analysis in Miyatake *et al.* [16], for the analysis setups that are denoted by the superscript "$*$" in the label (see Table I and main text explaining the table). We also consider the analyses using the different photo-z prior centered at $\Delta z_{\rm ph} = 0$, $\Pi(\Delta z_{\rm ph}) = \mathcal{N}(0, 0.1)$, to study the impact of the different priors of the photo-z error parameter on our results, as denoted by the superscript "†" in the label. The third column denotes the dimension of the sampled model parameters and the data vectors, $\mathcal{D}(\boldsymbol{\theta})$ and $\mathcal{D}(\boldsymbol{d})$, respectively.

Setup label	Description	$\mathcal{D}(\boldsymbol{\theta})$, $\mathcal{D}(\boldsymbol{d})$
3×2pt*	[*baseline analysis*] a joint analysis of $\Delta\Sigma$, $w_{\rm p}$ and $\xi_\pm$	16, 74
2×2pt*	A joint analysis of $\Delta\Sigma$ and $w_{\rm p}$	13, 59
Cosmic shear*	Cosmic shear analysis using $\xi_\pm$	10, 15
3×2pt, w/o LOWZ*	3×2pt, without LOWZ sample for $w_{\rm p}$ and $\Delta\Sigma$	14, 56
3×2pt, w/o CMASS1*	3×2pt, without CMASS1 sample for $w_{\rm p}$ and $\Delta\Sigma$	14, 55
3×2pt, w/o CMASS2*	3×2pt, without CMASS2 sample for $w_{\rm p}$ and $\Delta\Sigma$	14, 52
2×2pt, w/o LOWZ*	2×2pt, without LOWZ sample for $w_{\rm p}$ and $\Delta\Sigma$	11, 41
2×2pt, w/o CMASS1*	2×2pt, without CMASS1 sample for $w_{\rm p}$ and $\Delta\Sigma$	11, 40
2×2pt, w/o CMASS2*	2×2pt, without CMASS2 sample for $w_{\rm p}$ and $\Delta\Sigma$	11, 37
No photo-z error	3×2pt, fixing $\Delta z_{\rm ph} = 0$	15, 74
No shear error*	3×2pt, fixing $\Delta m = 0$	15, 74
No magnification bias error*	3×2pt, fixing $\alpha_{\rm mag} = \mu$	13, 74
No PSF error*	3×2pt, fixing $\alpha_{\rm psf} = \beta_{\rm psf} = 0$	14, 74
No IA*	3×2pt, fixing $A_{\rm IA} = 0$	15, 74
Extreme IA*	3×2pt, fixing $A_{\rm IA} = 5$	15, 74
$R_{\rm max} = 30h^{-1}$ Mpc*	3×2pt, using the $\Delta\Sigma$ and $w_{\rm p}$ signals up to $R \le R_{\rm max} = 30h^{-1}$ Mpc	16, 51
2cosmo*	3×2pt, varying only two cosmological parameters, $\Omega_{\rm de}$ and $\ln(10^{10}A_{\rm s})$	13, 74
2cosmo, 2×2pt*	2×2pt, varying only two cosmological parameters, $\Omega_{\rm de}$ and $\ln(10^{10}A_{\rm s})$	10, 59
$\Delta z_{\rm ph} \sim \mathcal{U}(-1, 1)$	3×2pt, with an uniform prior of $\Delta z_{\rm ph} \sim \mathcal{U}(-1, 1)$	16, 74
3×2pt†	3×2pt, with prior of $\Delta z_{\rm ph} \sim \mathcal{N}(0, 0.1)$	16, 74
2×2pt†	2×2pt, with prior of $\Delta z_{\rm ph} \sim \mathcal{N}(0, 0.1)$	16, 59
Cosmic shear†	Cosmic shear, with prior of $\Delta z_{\rm ph} \sim \mathcal{N}(0, 0.1)$	16, 15
XMM (33.17 deg^2)*	3×2pt, but using only XMM field for $\Delta\Sigma$ and $\xi_\pm$	16, 74
GAMA15H (40.87 deg^2)*	3×2pt, but using only GAMA15H field for $\Delta\Sigma$ and $\xi_\pm$	16, 74
HECTOMAP (43.09 deg^2)*	3×2pt, but using only HECTOMAP field for $\Delta\Sigma$ and $\xi_\pm$	16, 74
GAMA09H (78.85 deg^2)*	3×2pt, but using only GAMA09H field for $\Delta\Sigma$ and $\xi_\pm$	16, 74
VVDS (96.18 deg^2)*	3×2pt, but using only VVDS field for $\Delta\Sigma$ and $\xi_\pm$	16, 74
WIDE12H (121.32 deg^2)*	3×2pt, but using only WIDE12H field for $\Delta\Sigma$ and $\xi_\pm$	16, 74
w/o star weight	3×2pt, but without using star weight when computing $w_{\rm p}$	16, 74
DEMPZ & WX*	3×2pt, using DEMPZ & WX for $p_{\rm s}(z_{\rm s})$	16, 74
MIZUKI*	3×2pt, but using MIZUKI for the source selection and the stacked $p_{\rm s}(z_{\rm s})$	16, 74
DNNZ*	3×2pt, but using DNNZ for the source selection and the stacked $p_{\rm s}(z_{\rm s})$	16, 74

analysis method after unblinding. In the following text, we will explicitly indicate any analysis or results that were obtained after unblinding.

V. MODEL VALIDATION

In order to obtain unbiased cosmological parameters from the data, we need to validate our model. We adopt the minimal bias model for the galaxy bias, which was already validated using mock catalogs populated by galaxies using different models for the galaxy-halo connections in Sugiyama *et al.* [13] for the hypothetical HSC-Y1 mock data.

In addition to the galaxy bias uncertainties, we also validate the use of `halofit` for the prediction of cosmic shear signals, neglecting baryonic effects on the nonlinear matter power spectrum. To validate this, we simulate the data vectors using `HMCode` with various degrees of baryonic physics.

For the HSC-Y3 data, we have greater statistical constraining power due to three times larger area coverage than the HSC-Y1 data, and also due to the inclusion of cosmic shear in the 3×2pt analysis compared to the HSC-Y1 2×2pt analysis [6]. Therefore, we subject our modeling and analysis methods to validation tests using the mock data vectors, but using the covariance matrix for the HSC-Y3 data.

In this paper, we use an informative prior on $\Delta z_{\rm ph}$ taken from the result of the small-scale 3×2pt analysis, which can more precisely self-calibrate $\Delta z_{\rm ph}$ due to its higher signal-to-noise ratio. We validate the use of the posterior from the small-scale analysis as a prior on $\Delta z_{\rm ph}$ by analyzing a mock data vector that includes the photo-z bias effect.

We describe the model validation results in Appendix V in detail. In brief summary, the validation tests are passed for most of the synthetic data vectors; our method can recover the input S_8 with a bias smaller than 0.5σ (σ is the marginalized error for the baseline 3×2pt analysis), where we test our method using the mode value of S_8 in the posterior, rather than the MAP value, compared to the input value used in generating the synthetic data. However, given the fact that there is no established, accurate theory of the galaxy formation physics or galaxy-halo connection, we also consider the worst-case scenario in order for us to be ready for any unexpected result in the cosmological parameter estimation. As for the worst-case scenario, we consider the extreme mock data of SDSS galaxies, where we consider a nonstandard prescription of the galaxy-halo connection when generating the mock SDSS catalogs from N-body simulations. Even for these extreme mocks, the minimal bias model can recover the input S_8 value with a bias $\lesssim1\sigma$, while the halo model method suffers from a greater bias. For these worst-case cases, we have a diagnostic to identify a signature of the strong nonlinearities in the galaxy-halo connection. Since changes in the galaxy-halo connection cause a stronger modification in the clustering observables at smaller scales around and below virial radii of massive halos (Mpc scales), while the clustering observables have the linear theory limit on sufficiently large scales, which is captured by the minimal bias model. Hence, if the actual SDSS galaxies are affected by such extreme galaxy-halo connection, the cosmological parameters display systematic shifts with changing the scales cuts from small to large scales in the cosmology inference. We carefully study these behaviors using the different mocks. For the actual cosmology analysis of the HSC-Y3 and SDSS data, we did not observe such a systematic change in the S_8 values for the different scales cuts or from the small- and large-scale 3×2pt analyses. These tests gave us a justification that we can unblind the results.

VI. RESULTS

A. HSC-Y3 ΛCDM constraint

In this section, we present the main results from the cosmological parameter inference using the HSC-Y3 lensing and SDSS clustering measurements for the flat ΛCDM model. All of the analyses in this section were done before unblinding, and the results are presented without any change after unblinding.

Figure 1 shows the cosmological constraints from the large-scale 3×2pt analysis carried out in this paper. The central values and associated errors are

$$\begin{aligned}\Omega_{\rm m} &= 0.401^{+0.056}_{-0.064}(0.394),\\ \sigma_8 &= 0.666^{+0.069}_{-0.051}(0.705),\\ S_8 &= 0.775^{+0.043}_{-0.038}(0.808).\end{aligned}\tag{35}$$

The HSC-Y3 large-scale 3×2pt analysis achieves $\sim5\%$ fractional accuracy on S_8. The improvement in the statistical precision of S_8 compared to the HSC-Y1 2×2pt analysis is a factor of ~2, due to the increase in the HSC survey area and the inclusion of the cosmic shear data.

Figure 2 shows how the cosmological parameter constraints are improved by combining the 2×2pt and cosmic shear analysis in 3×2pt. It is clear that the 2×2pt analysis and cosmic shear are complementary to each other for constraining the cosmological parameters; combining them improves the S_8 constraint. Note that the cosmic shear analysis alone cannot constrain $\Omega_{\rm m}$, because the cosmic shear in this paper does not include tomographic information and therefore is not sensitive to the growth history of matter clustering, which depends on $\Omega_{\rm m}$.

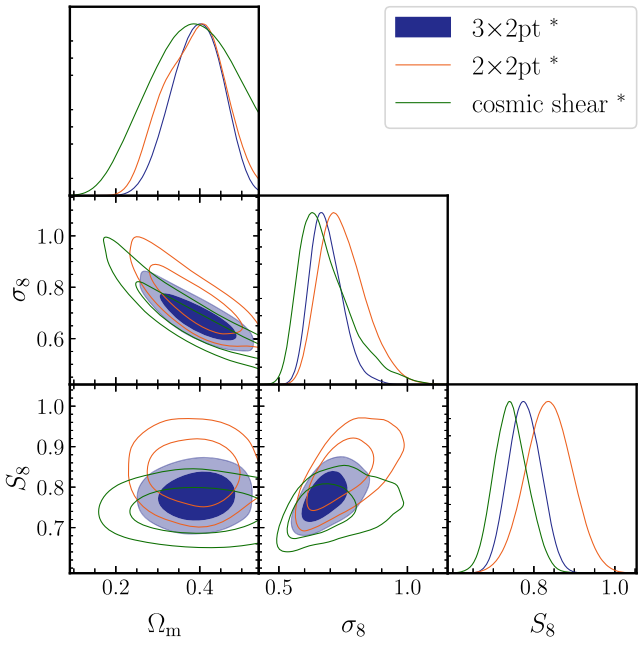

FIG. 2. The cosmological parameter constraints for the baseline 3×2pt, 2×2pt, and cosmic shear analyses. Here, every analysis uses the informative prior on Δz_{ph} from the HSC-Y3 small-scale analysis by Miyatake *et al.* [16].

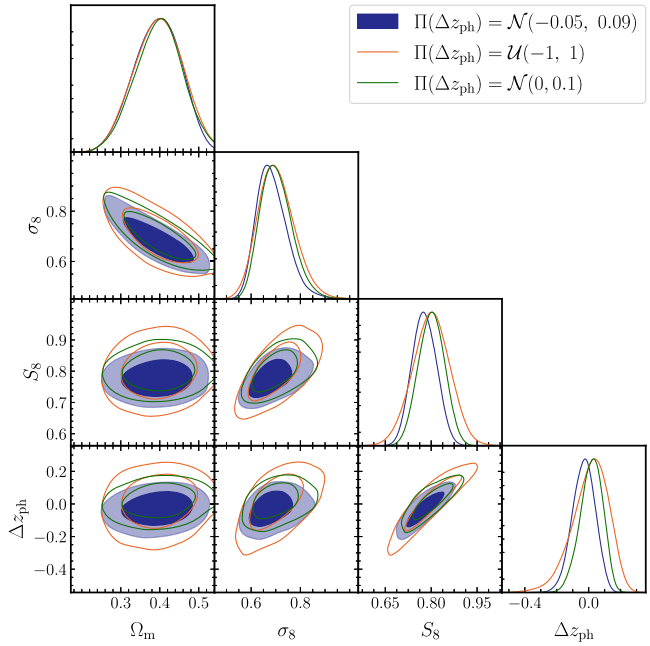

FIG. 3. Cosmological parameter constraints for HSC-Y3 3×2pt analyses with three different Δz_{ph} prior choices; the informative prior taken from the fiducial small-scale analysis result, the uninformative prior $\mathcal{U}(-1, 1)$, and the informative prior $\Pi(\Delta z_{ph}) = \mathcal{N}(0, 0.1)$.

Figure 3 shows the result of the 3×2pt analyses for three cosmological parameters and the Δz_{ph} parameter, using three different Δz_{ph} priors: the informative prior taken from the baseline small-scale analysis result, the uninformative prior, $\Pi(\Delta z_{ph}) = \mathcal{U}(-1, 1)$, and the informative Gaussian prior with little room for a large shift from zero, $\Pi(\Delta z_{ph}) = \mathcal{N}(0, 0.1)$. In the baseline analysis of this paper, we use the first prior. Comparing the results with $\mathcal{N}(-0.05, 0.09)$ and $\mathcal{N}(0, 0.1)$ tells us the impact of the central value of the Gaussian prior on the cosmological parameters. When the uninformative prior is used, the large-scale 3×2pt analysis has insufficient information to constrain Δz_{ph}, although the posterior of Δz_{ph} prefers a negative value of Δz_p as found in the small-scale 3×2pt analysis. As a result, the S_8 constraint is significantly degraded. This was the main reason that we decided to use the informative prior obtained from the baseline small-scale 3×2pt analysis in Miyatake *et al.* [16] as shown in the blue contour. This prior choice was made during the blind analysis phase, and therefore the baseline result is free of confirmation bias.

From Fig. 3, we find that adopting the informative Gaussian prior around $\Delta z_{ph} = 0$ results in a larger S_8 value. The shift in S_8 between the baseline analysis and the Gaussian prior of Δz_{ph} in this case corresponds to a shift of 0.7σ, a non-negligible amount. In Appendix A, we validated the use of the posterior obtained from the small-scale 3×2pt analysis as the prior on Δz_{ph} using the mock analysis. We found that the posterior of Δz_{ph} from the small-scale analysis can be safely used as the prior in the large-scale 3×2pt analysis, i.e., the analysis in this paper, to recover the input S_8 value. Thus, we decided prior to unblinding to adopt the informative prior of $\mathcal{N}(-0.05, 0.09)$ for our baseline analysis.

Figure 4 compares the model predictions at the MAP (maximum *a posteriori*) model of the chain with the measured signals. The best-fit model fairly well reproduces the measured signals over the range of separations used for the cosmological analysis. The figure also shows that the best-fit model fails to reproduce the measured w_p and $\Delta\Sigma$ on scales below the fitting range. This is expected, as the simple minimum bias model is invalid on such small scales.

Figure 5 shows the goodness-of-fit test of the 3×2pt analysis. To quantitatively evaluate the goodness-of-fit, we follow the same method as for the S16A analysis [6]; we simulate 100 noisy mock data vectors, apply the same analysis to each mock data vector as for the real data, and obtain the distribution of the χ^2 values at the MAP model for each mock. Note that here we generate the noisy data vector using the covariance matrix with a multiplicative shear bias parameter of $m = 0$ as described in Appendix V. We find that the probability to exceed the observed value, $\chi^2 \simeq 70$, by chance is $p = 0.43$. We have also checked that the dependence of the reference χ^2 distribution on the assumed multiplicative shear bias value used when

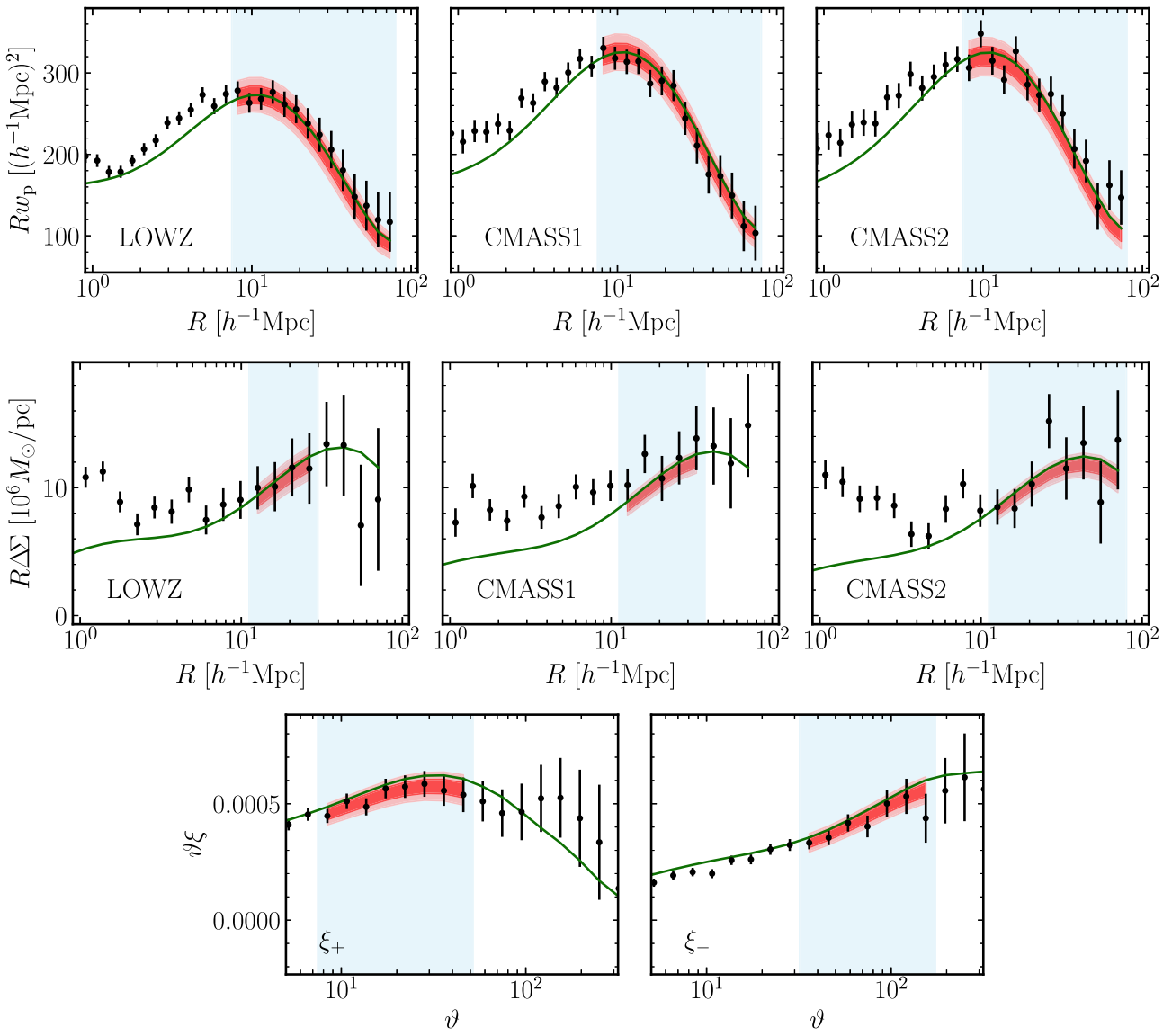

FIG. 4. Comparison between the measured signals and the best-fit model predictions for the baseline large-scale 3×2pt analysis. From the top to the bottom panels, we show the comparison for $w_{\rm p}(R)$ and $\Delta\Sigma(R)$ for the three SDSS samples (LOWZ, CMASS1, and CMASS2), and the cosmic shear correlation functions, $\xi_\pm(\vartheta)$, respectively. In each panel, the black points with error bars denote the measured signals in each R or ϑ bin, where the error bar is computed from the diagonal component of the covariance matrix. The solid line denotes the model prediction at the MAP (maximum *a posteriori* model of the chain), while the red-shaded regions show the 68% and 95% credible intervals of the model predictions in each bin. The blue shaded region in each panel indicates the range of R or ϑ that is used for the cosmological parameter inference in this paper. See Sec. III for details of the model predictions. Note that the x-axes in the top and middle panels are the comoving distance in the reference cosmology (see the main text), $R^{\rm ref}$, but we omit the superscript "ref" for simplicity.

generating the noisy mock data is weak and does not change our conclusion. We therefore conclude that within the statistical constraining power of our data, the model is able to describe the data with no signs of model misspecification.

B. Internal consistency

In this section, we present the results of internal consistency tests of our analysis. The analysis setups for the internal consistency tests are summarized in Table II. Figure 6 summarizes the result of the internal consistency tests, and Table IV in Appendix C summarizes the central values and credible intervals for each parameter. In short, we did not find any significant shift in each of the cosmological parameters compared to the expected statistical scatter.

The largest variation is the difference between the S_8 values obtained from the 2×2pt analysis versus from the cosmic shear analysis alone. First, the trends in S_8—i.e., the

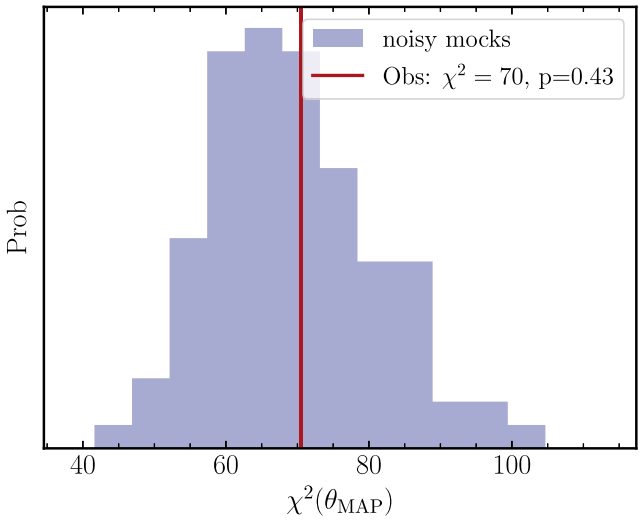

FIG. 5. The evaluation of the goodness-of-fit with the $\chi^2(\theta_{\rm MAP})$ value at the maximum *a posteriori* (MAP) model. The reference distribution (blue histogram) is obtained by analyzing 100 noisy mock data vectors. See the main text for how the noisy mock data vectors are generated. The vertical solid line denotes the observed χ^2 value for the cosmology analysis of the actual HSC-Y3 and SDSS data. The probability of finding the χ^2 value larger than the observed value (p value) is about 43%.

larger and smaller S_8 values for the two analyses than the S_8 value from the 3×2pt analysis—are also found in the model validation tests as shown in Fig. 8. To make a quantitative estimate of the statistical significance of the S_8 difference, ΔS_8, we use the same 100 noisy mock realizations of the vector as those used in the goodness-of-fit analysis. We run the 2×2pt and cosmic shear analyses for each noisy mock realization and then assess how often the measured difference in S_8 from the real data occurs in the distribution of the S_8 difference measured in the 100 noisy mock realizations. The left panel of Fig. 7 shows that the probability to exceed the observed value $\Delta S_8 = 0.10$ by chance is $p = 0.2$.

As another internal consistency test, we compare our result with that from the HSC-Y3 small-scale 3×2pt analysis in Miyatake *et al.* [16] as shown in Fig. 1. The two 3×2pt analyses use the same observables albeit on different ranges of scales, but use different theoretical model templates for the cosmology analysis; the minimal bias model in this paper and the emulator-based halo model in Miyatake *et al.* [16]. The figure shows that our result is in good agreement with that in Miyatake *et al.* [16]. In order to assess the consistency of these two analyses, we again used the 100 mocks, which allow us to account for the correlations between the cosmological parameters from the large- and small-scale 3×2pt analyses. As shown in the right panel of Fig. 7, the probability to observe an S_8 difference larger than what we obtain $\Delta S_8 \simeq 0.01$, is $p = 0.5$. Thus, we conclude that the large- and small-scale 3×2pt analyses are consistent with each other. The two vertical arrows in the right panel of Fig. 7 indicate the expected size of ΔS_8 in the presence of assembly bias effects that are simulated using the mock catalogs in Miyatake *et al.* [14]. The `assembly-b-ext` is the worst-case scenario of the assembly bias effect and can be flagged at a 2σ level if such effect really exists (see Sec. A for the detail of the mocks). The agreement between the results from the large-scale and small-scale analyses also indicates that the SDSS galaxies in our sample are not largely affected by the possible assembly bias effect [5,14].

C. Comparison with external data and S_8 tension

In Fig. 1 we also compare our result with external experiments. For the CMB, we consider the *Planck* 2018 [9] cosmological constraints—in particular, those derived from primary CMB information, referred to as "TT, EE, TE + lowE" in their paper.[4] For the lensing experiments, we use the cosmological constraints from DES-Y3 [70] and KiDS-1000 [8]. In particular, we use the cosmological constraint from a 3×2pt analysis with the MagLim sample from DES-Y3 data.[5] The fiducial KiDS-1000 3×2pt analysis included the angular diameter distance from the measured BAO scale in addition to the clustering information, which well constrains $\Omega_{\rm m}$ for the flat ΛCDM model. Hence, we instead compare with the result from the cosmic shear and galaxy-galaxy lensing (CS + GGL) analysis.[6]

Our result is generally in good agreement with both the DES-Y3 and KiDS-1000 results. For our result, the degeneracy direction in cosmological parameter subspaces such as the $\Omega_{\rm m}$-S_8 plane is slightly different from those of the DES-Y3 and KiDS-1000 results.

When comparing our result to the *Planck* 2018 result, we did not find any significant tension in the cosmological parameters. More quantitatively, we compare the cosmological parameter constraints from this paper and the *Planck* 2018 using the eigen tension metric [71]. We first identify the eigenmodes of the cosmological parameters by diagonalizing the posterior covariance. We found that the first two eigenmodes, $e_1 \equiv \sigma_8(\Omega_{\rm m})^{0.52}$ and $e_2 \equiv \Omega_{\rm m}(\sigma_8)^{-0.52}$ are well-constrained compared to the prior distribution. For this reason we use these eigenmodes for tension assessment. As an independent criterion of principle eigenmodes, we

[4]We use the Planck 2018 public chain of "base/plikHM_TTTEEE_lowl_lowE/base_plikHM_TTTEEE_lowl_lowE" downloaded from their wiki https://pla.esac.esa.int/pla/aio/product-action?COSMOLOGY.FILE_ID=COM_CosmoParams_fullGrid_R3.01.zip.

[5]We use the DES-Y3 public chain of "chain_3x2pt_lcdm_SR_maglim.txt" downloaded from DES Data Management: https://des.ncsa.illinois.edu/releases/y3a2/Y3key-products.

[6]We use the KiDS-1000 public chain of "samples_multinest_blindC_EE_nE_w.txt" downloaded from their website https://kids.strw.leidenuniv.nl/DR4/KiDS-1000_3x2pt_Cosmology.php.

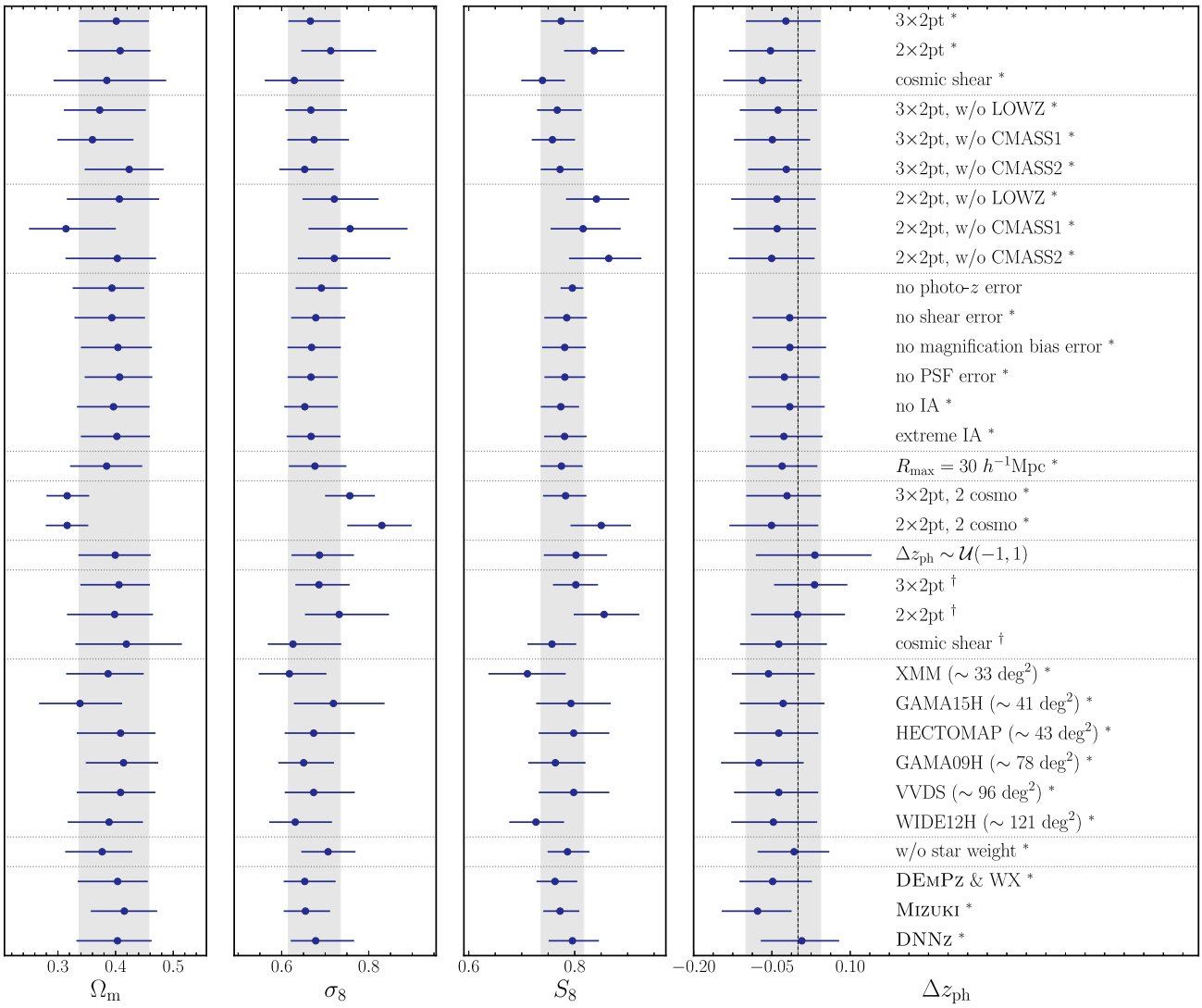

FIG. 6. Summary of internal consistency tests. The estimates of cosmological parameters, $\Omega_{\rm m}$, σ_8, and S_8, and the photo-z parameter, $\Delta z_{\rm ph}$, are summarized for each of the analysis setups in Table II. Here, the central point is the mode and the error bar is the 68% highest density interval estimated from the one-dimensional posterior distribution of each parameter. For comparison, the shaded band is the constraint from the baseline analysis. The vertical black dotted line in the $\Delta z_{\rm ph}$ panel denotes $\Delta z_{\rm ph} = 0$.

also computed the effective number of cosmological parameters constrained by the large-scale analysis using the Gaussian linear model [72]. Focusing only on the cosmological parameters, we find that the effective number of constrained cosmological model parameters is 1.99, which supports the choice to use the first two eigenmodes for tension assessment. For these eigenmodes, we estimate the parameter difference distribution, $P(\Delta \boldsymbol{e})$, from the MCMC of HSC-Y3 and Planck 2018, where $\Delta \boldsymbol{e} \equiv \boldsymbol{e}_{\rm HSC-Y3} - \boldsymbol{e}_{\rm Planck}$. We then compute the p-value of the null hypothesis, i.e., the case that the *Planck 2018* and HSC-Y3 results are in perfect agreement with each other,

$$p = \int_{P(\Delta \boldsymbol{e}) < P(\boldsymbol{0})} \mathrm{d}(\Delta \boldsymbol{e}) P(\Delta \boldsymbol{e}). \tag{36}$$

We find $p = 0.846$, corresponding to at most a 1.4σ-level difference between our HSC-Y3 result and the *Planck* result. Therefore we conclude that our result is consistent with the *Planck* CMB results. Although at face value this seems different from the 2.5σ tension between *Planck* and the small-scale HSC-Y3 result presented in Miyatake *et al.* [16], this difference is entirely due to the lesser statistical constraining power of our result, as reflected in the larger credible intervals.

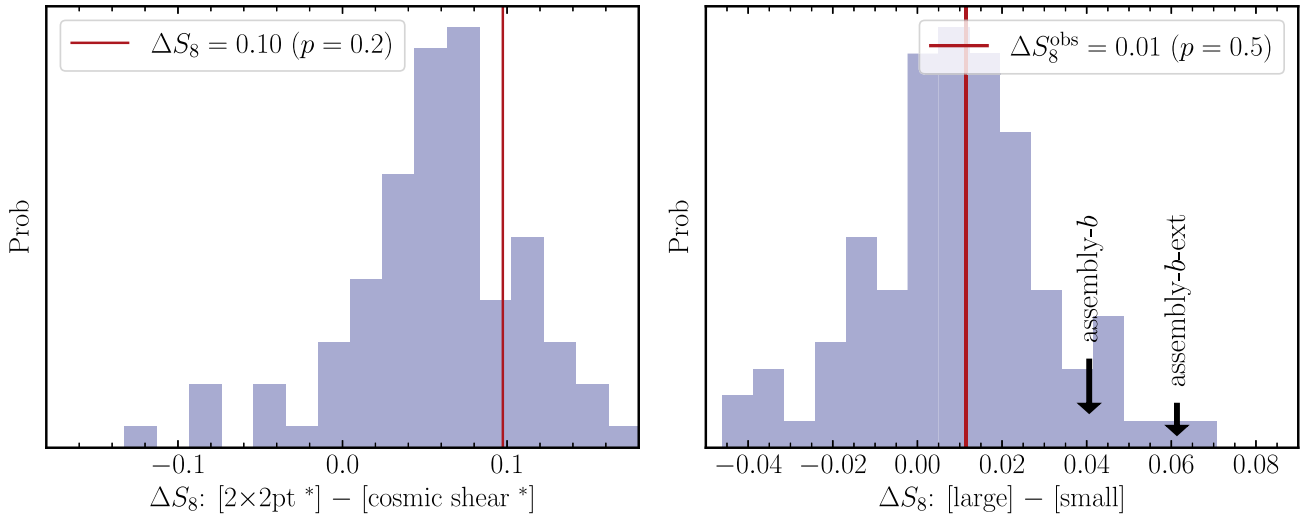

FIG. 7. A statistical significance of the difference between the S_8 values from the two analyses, where we define ΔS_8 by the difference between the S_8 modes values in the 1D posteriors of the two analyses. *Left panel*: The result for ΔS_8 between the large-scale 2×2pt and cosmic shear analyses. The blue histogram denotes the distribution of ΔS_8 that is obtained by carrying out these analyses on each of 100 realizations of the noisy mock data vector (see text for details). The red solid line is the observed $\Delta S_8 = 0.10$ in the real data. The p-value is $p = 0.2$. *Right panel*: The result for ΔS_8 between the large-scale 3×2pt analysis in this paper and the small-scale 3×2pt analysis in the companion paper by Miyatake *et al.* [16]. The observed difference is $\Delta S_8 = 0.01$ and the probability to exceed this value by chance is $p = 0.5$. The two arrows indicated by "assembly-b" and "assembly-b-ext" denote the expected difference values of S_8 obtained from the simulated synthetic data, where the assembly bias effects with different amplitudes are included.

VII. CONCLUSION

In this paper, we have presented cosmological constraints from a joint analysis of galaxy clustering ($w_{\rm p}$), galaxy-galaxy lensing ($\Delta\Sigma$), and the cosmic shear correlation ($\xi_\pm$), measured from the HSC-Y3 shape catalog and the SDSS DR11 spectroscopic galaxy catalog. We have adopted a conservative analysis strategy: we employed the "minimal bias model" as a theoretical template to model $\Delta\Sigma$ and $w_{\rm p}$, and strict scale cuts to ensure its validity. Using mock data vectors, we showed that the minimal bias model can recover the input cosmological parameter to within the statistical error for the HSC-Y3 data, as long as the analysis is restricted to large scales, $R > 8$ and $12h^{-1}$ Mpc for $w_{\rm p}$ and $\Delta\Sigma$, respectively. This is because structure formation on such large scales is governed by gravity alone whereas the nonlinear galaxy bias and baryonic effects are confined to smaller scales. In addition, we employed a conservative prior on the nuisance parameter, $\Delta z_{\rm ph}$, to model a residual systematic effect in the mean redshift of HSC source galaxies used in the weak-lensing measurements. We adopted a Gaussian prior of $\Delta z_{\rm ph}$ given by $\mathcal{N}(-0.09, 0.05)$, based on a similar 3×2pt analysis in the companion paper Miyatake *et al.* [16] using the same data vector down to smaller scales. Another key feature of this analysis is that we do not include the tomographic information in weak-lensing signals, but rather adopt a a single conservatively-selected source sample to make our results robust against the residual photo-z error following the method in Oguri and Takada [53].

Our cosmological parameter constraint for the flat ΛCDM model is $S_8 = 0.775^{+0.043}_{-0.038}$, with ∼5% precision. From the comparison with *Planck* 2018 [9], we found that our result is consistent with *Planck*, indicating no significant tension. We found that the cosmic shear correlation function not only improves the cosmological parameter estimation, but also helps to calibrate the residual photo-z error $\Delta z_{\rm ph}$. If we employ a prior on $\Delta z_{\rm ph}$ centered at no bias value, $\mathcal{N}(0, 0.1)$, the S_8 value is shifted to a higher value by $\sim 1\sigma$. Hence we concluded that a treatment of $\Delta z_{\rm ph}$ is important for our cosmological analysis. We emphasize that, using various validation tests, we defined the analysis setups and methods during the blinding analysis stage. Using the 100 noisy mock analyses, we confirmed that the main result of the large-scale analysis in this paper is statistically consistent with the small-scale analysis in Miyatake *et al.* [16].

The constraining power of the large-scale 3×2pt analysis in this paper is weaker than the *Planck* 2018 result. Increasing the statistical constraining power is important for a stringent test of the S_8 tension or, more generally, the ΛCDM model. There are several ways to improve the statistical constraints from the large-scale analysis. First, in future, we will use the full data of the HSC survey covering about $1,100$ deg^2 of sky to carry out a similar 3×2pt analysis. Second, we can include tomographic cosmic shear tomography information in the 3×2pt analysis. As shown in Li *et al.* [18] and Dalal *et al.* [19], the cosmic shear tomography can self-calibrate the residual photo-z

error; therefore, we expect that adding cosmic shear tomography to the large-scale 2×2pt signals can improve the cosmological constraints as well as the residual photo-z error calibration. Third, to improve the cosmological constraint, we could push the scale cuts down to smaller scales. In order to use the smaller scale signals of $w_{\rm p}$ or $\Delta\Sigma$, we would need to account for the nonlinear physics in the $R \lesssim 10h^{-1}$ Mpc regime, which would require more complicated modeling of galaxy bias than the minimal bias model. We will leave these improvements to our future studies.

ACKNOWLEDGMENTS

This work was supported in part by World Premier International Research Center Initiative (WPI Initiative), MEXT, Japan, and JSPS KAKENHI Grants No. JP18H04350, No. JP18H04358, No. JP19H00677, No. JP19K14767, No. JP20H00181, No. JP20H01932, No. JP20H04723, No. JP20H05850, No. JP20H05855, No. JP20H05856, No. JP20H05861, No. JP21J00011, No. JP21H05456, No. JP21J10314, No. JP21H01081, No. JP21H05456, No. JP22K03634, No. JP22K03655, No. JP22K21349, No. JP23H00108, and No. JP23H04005 by Japan Science and Technology Agency (JST) CREST JPMHCR1414, by JST AIP Acceleration Research Grant No. JP20317829, Japan, and by Basic Research Grant (Super AI) of Institute for AI and Beyond of the University of Tokyo. S. S. was supported in part by International Graduate Program for Excellence in Earth-Space Science (IGPEES), WINGS Program, the University of Tokyo. Y. K. is supported in part by the David and Lucile Packard foundation. R. D. acknowledges support from the NSF Graduate Research Fellowship Program under Grant No. DGE-2039656. R. M. is supported by a grant from the Simons Foundation (Simons Investigator in Astrophysics, Award ID No. 620789). The Hyper Suprime-Cam (HSC) collaboration includes the astronomical communities of Japan and Taiwan, and Princeton University. The HSC instrumentation and software were developed by the National Astronomical Observatory of Japan (NAOJ), the Kavli Institute for the Physics and Mathematics of the Universe (Kavli IPMU), the University of Tokyo, the High Energy Accelerator Research Organization (KEK), the Academia Sinica Institute for Astronomy and Astrophysics in Taiwan (ASIAA), and Princeton University. Funding was contributed by the FIRST program from Japanese Cabinet Office, the Ministry of Education, Culture, Sports, Science and Technology (MEXT), the Japan Society for the Promotion of Science (JSPS), Japan Science and Technology Agency (JST), the Toray Science Foundation, NAOJ, Kavli IPMU, KEK, ASIAA, and Princeton University. This paper makes use of software developed for the Vera C. Rubin Observatory. We thank the Rubin Observatory for making their code available as free software at [73]. The Pan-STARRS1 Surveys (PS1) have been made possible through contributions of the Institute for Astronomy, the University of Hawaii, the Pan-STARRS Project Office, the Max-Planck Society and its participating institutes, the Max Planck Institute for Astronomy, Heidelberg and the Max Planck Institute for Extraterrestrial Physics, Garching, The Johns Hopkins University, Durham University, the University of Edinburgh, Queen's University Belfast, the Harvard-Smithsonian Center for Astrophysics, the Las Cumbres Observatory Global Telescope Network Incorporated, the National Central University of Taiwan, the Space Telescope Science Institute, the National Aeronautics and Space Administration under Grant No. NNX08AR22G issued through the Planetary Science Division of the NASA Science Mission Directorate, the National Science Foundation under Grant No. AST-1238877, the University of Maryland, and Eotvos Lorand University (ELTE) and the Los Alamos National Laboratory. Based in part on data collected at the Subaru Telescope and retrieved from the HSC data archive system, which is operated by Subaru Telescope and Astronomy Data Center at National Astronomical Observatory of Japan.

APPENDIX A: MODEL VALIDATION

In this appendix, we validate the model and the analysis setup we adopted for the HSC-Y3 real data analysis. To validate the baseline choice of model and setup in this paper, we generate various kinds of data vectors which include systematic errors. We analyze each of the contaminated data vectors with the baseline model and setup; checking whether the cosmological parameter constraints are robust given the constraining power of HSC-Y3 data allows us to validate our modeling framework. We first make a fiducial mock which does not include any systematic errors, and then add simulated systematic errors of various types to the fiducial mock. We categorize the simulated systematic errors on the data vectors into four groups, as described in the following subsections.

The galaxy-galaxy lensing and galaxy clustering signals in the fiducial mock is the same as used in the HSC-Y1 analysis of Sugiyama *et al.* [13] and Miyatake *et al.* [14]. These are measured from the galaxy distribution populated by an HOD prescription on halos identified in N-body simulation data. The cosmic shear signal is generated from the `halofit` [47] code, updated by Takahashi *et al.* [48]. To simulate the data vector, we use the Planck 2015 cosmology [74].

Table III summarizes the validation tests done in the following subsections, and the results are summarized in Fig. 8.

1. Generation of contaminated mock data vectors

a. Galaxy bias uncertainties

Galaxies are biased tracers of the underlying matter field, and thus we can extract the cosmological information only after marginalizing over galaxy bias uncertainty.

TABLE III. A summary of mock signals used for the validation tests. Please see Miyatake *et al.* [14] for the details of each mock catalogs which are used to simulate the synthetic data of $\Delta\Sigma$ and $w_{\rm p}$.

Setup label	Description
Fiducial mock analyses	
3×2pt	3×2pt analysis using clustering, galaxy-galaxy lensing and cosmic shear
2×2pt	2×2pt analysis using clustering and galaxy-galaxy lensing
Cosmic shear	Cosmic shear analysis
Effects of galaxy bias uncertainties on $w_{\rm p}$ and $\Delta\Sigma$	
sat-mod, sat-DM, sat-sub	Use different ways to populate satellite galaxies into host halos
Off centering 1, 2, 3, 4	Mocks include the off-centering effects of central galaxies
Baryon	Mock includes baryonic feedback effect
Assembly-*b*-ext	Mock includes the extremely large assembly bias effect
Assembly-*b*	Mock includes the large assembly bias effect
Cent-incomp	Mock includes the incompleteness effect of central galaxies
fof	Mock uses fof halos to populate galaxies
Baryonic effect on cosmic shear $\xi_\pm$	
HMCode v2015 (DM only)	Mock cosmic shear is generated by HMCode v2015 with $A_{\rm bary}=3.13$
HMCode v2015 ($A_{\rm bary}$)	Mock cosmic shear is generated by HMCode v2015 with $A_{\rm bary}\in[2.8,1.6]$
HMCode v2020 ($T_{\rm TGN}$)	Mock cosmic shear is generated by HMCode v2020 with $T_{\rm AGN}\in[7.3,8.3]$
Photo-z bias on $\Delta\Sigma$ and $\xi_\pm$	
$\Delta z^{\rm in}_{\rm ph}=-0.2$	Mock signals include the effect of the worst-case photo-z error: $\Delta z^{\rm in}_{\rm ph}=-0.2$
PSF systematics on $\xi_\pm$	
PSF 4th	Mock signals include the measured PSF systematic effects up to the fourth moments of PSF

At cosmological scales, gravity is the only force that drives structure formation, and hence the cosmological perturbation theory of structure formation and the galaxy bias expansion based on perturbation theory should work well. However, at quasinonlinear scales, perturbation theory and the galaxy bias expansion break down due to nonlinear physics.

In this paper, we analyze the galaxy clustering signal $w_{\rm p}$ at $R>8h^{-1}$ Mpc, and the galaxy-galaxy lensing signal $\Delta\Sigma$ at $R>12h^{-1}$ Mpc, using the minimal bias model based on cosmological perturbation theory. We validated the use of the minimal bias model using the same scale cuts as those in Sugiyama *et al.* [13], which checked that the minimal bias model can recover cosmological parameters within the HSC-Y1 statistical error. In this HSC-Y3 3×2pt analysis, we have higher statistical power than HSC-Y1 due to the larger area coverage of the HSC-Y3 shape catalog and the inclusion of the cosmic shear signal. Therefore, we repeat the validation of the minimal bias model as in Sugiyama *et al.* [13] using the HSC-Y3 covariance matrix.

b. Baryonic effects on cosmic shear

For the evaluation of the cosmic shear signal, we use `halofit` [47] updated by Takahashi *et al.* [48] as the fiducial modeling method to compute the nonlinear matter power spectrum for an input model.

The calibration of the fitting formula, `halofit`, was obtained using N-body simulations for ΛCDM cosmologies. However, baryonic effects inherent in galaxy formation physics alter the total matter power spectrum at nonlinear scales, $k\gtrsim0.1h$ Mpc^{-1}, as shown by hydrodynamical simulations e.g., [75]. To validate the use of `halofit`, which does not include baryonic feedback effects, we generate mock data vectors in which we simulate the baryonic effects on the power spectrum for a given cosmological model using the 2015 and 2020 versions of `HMCode` [76].[7] In `HMCode-2015` [77], the baryonic effect is parametrized by the halo concentration parameter $A_{\rm bary}$. $A_{\rm bary}=3.13$ corresponds to the case of no baryonic effects, i.e., dark matter only case. The smaller values of $A_{\rm bary}$ correspond to the case where the baryonic effects are greater. For our validation tests we consider $A_{\rm bary}=3.13$, 2.8, 2.5, 2.2, 1.9, and 1.6. The most extreme value we assume, $A_{\rm bary}=1.6$, is designed to reproduce the OWLS simulation result [78]. In `HMCode-2020` [76], the parameter $\log_{10}(T_{\rm AGN}/{\rm K})$ is used to model the AGN feedback effect on the matter power spectrum, and we use $\log_{10}(T_{\rm AGN}/{\rm K})=7.3$, 7.5, 7.7, 7.9, 8.1, and 8.3 for the baryon-affected mocks. Here, $\log_{10}(T_{\rm AGN}/{\rm K})=7.6$ (8.3) is designed to reproduce the AGN feedback effects in the `BAHAMAS` [79] (`COSMO-OWLS` [80]) simulations.

[7]In the tomographic cosmic shear analyses with HSC-Y3 data by Li *et al.* [18] and Dalal *et al.* [19], we use the 2016 version of `HMCode` instead of the 2015 version used in this paper. The 2016 version of `HMCode` is an extension of the 2015 version of `HMcode` to the beyond ΛCDM model, e.g., dark energy, neutrino mass, and modified gravity. Thus, there is no difference between the two versions used in Li *et al.* [18] or Dalal *et al.* [19] and this paper as long as we focus on ΛCDM model.

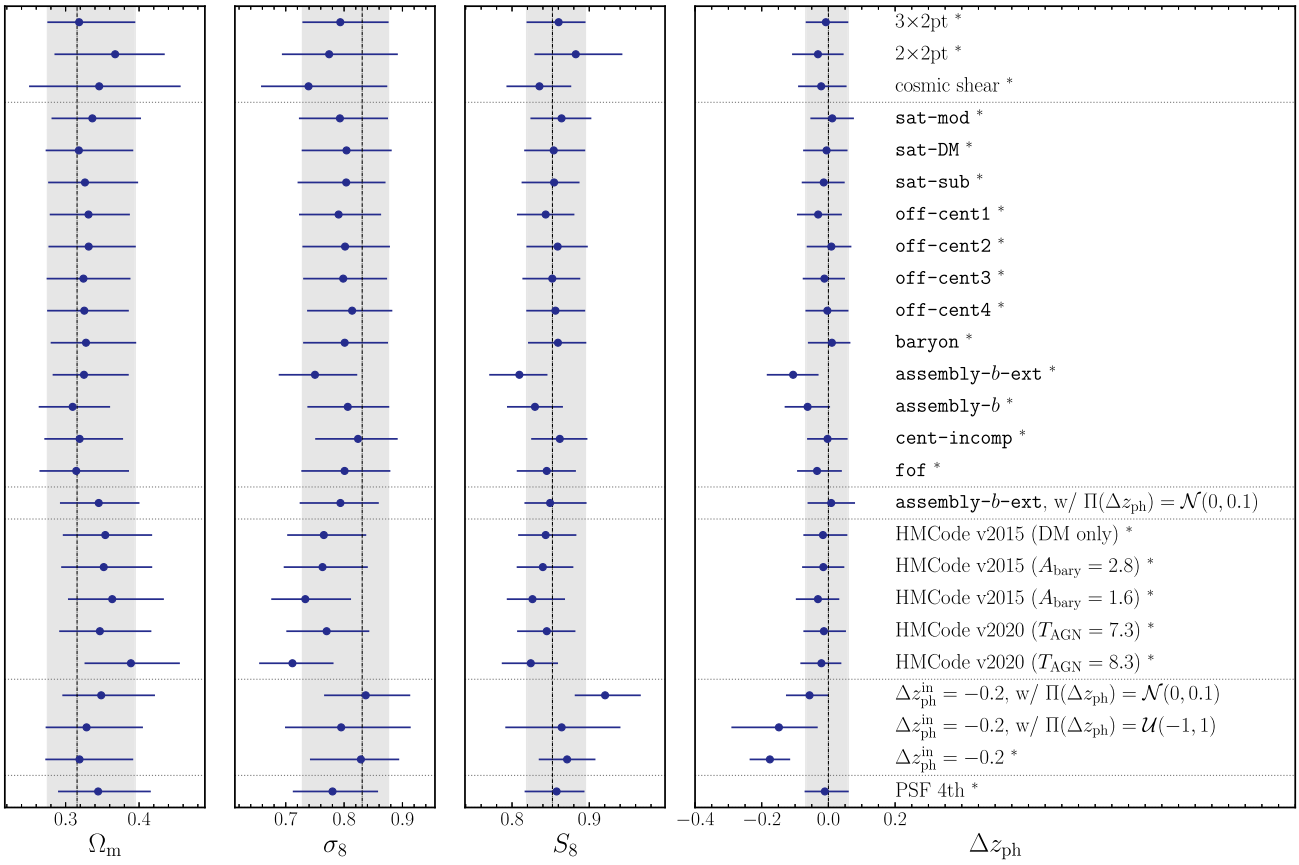

FIG. 8. Summary of the validation tests of the model and method. We apply the baseline analysis method to the synthetic data vectors in Table III to obtain constraints on the three cosmological parameters, Ω_m, σ_8, and S_8, and the photo-z parameter Δz_{ph}. Similar types of validation tests are grouped by horizontal dotted lines. The superscript "$*$" denotes the analysis using the informative prior of Δz_{ph} that is taken from the posterior distribution of the small-scale 3×2pt analysis in Miyatake *et al.* [16] on the same synthetic data vector. The top section shows the results of the baseline analysis on the fiducial mock, i.e., the data vector uncontaminated by systematic effects. The second section shows the robustness of the minimum bias model against uncertainties in the galaxy bias or the galaxy-halo connection, where we use the different SDSS galaxy mock catalogs to simulate $\Delta\Sigma$ and w_p affected by the different galaxy-halo connections. The row "assembly-b-ext w $\Pi(\Delta z_{ph} = \mathcal{N}(0.1)$" shows the result obtained using the synthetic data for the "assembly-b-ext" mock, but using the informative Gaussian prior on Δz_{ph} given by $\Pi(\Delta z_{ph}) = \mathcal{N}(0, 0.1)$. The fourth section shows the validation of the model of cosmic shear signal against baryonic effect contamination simulated by different versions of `HMCode`. The fifth section shows the results for the validation tests using the synthetic data that is affected by a systematic error in the mean source redshift by $|\Delta z_{ph}^{in}| = 0.2$ (see text for details). Here $|\Delta z_{ph}^{in}| = 0.2$ gives the worst-case scenario for the effect of the unknown systematic photo-z error, because the small-scale 3×2pt has the precision of $\sigma(\Delta z_{ph}) \sim 0.1$ for the calibration of the photo-z error parameter. The analysis with superscript "$*$" uses the informative prior of Δz_{ph} taken from the small-scale 3×2pt analysis on the same synthetic data (that is, this is our baseline analysis method). The analysis with the labels "$\Pi(\Delta z_{ph} = \mathcal{N}(0, 0.1)$" shows the result using the informative Gaussian prior around $\Delta z_{ph} = 0$, and "$\Pi(\Delta z_{ph} = \mathcal{U}(-1, 1)$" shows the result using the uninformative flat prior. The last section is the validation of our PSF systematics modeling in which the synthetic cosmic shear signals include the PSF systematics up to the fourth moment of PSF.

c. A systematic error in the mean source redshift

The small-scale 3×2pt analysis by Miyatake *et al.* [16] uses a uniform prior to self-calibrate the residual systematic error in the source redshift, Δz_{ph}. In this paper we use the same source sample, and use the mode and the credible interval of Δz_{ph} from Miyatake *et al.* [16] as an informative prior on Δz_{ph} in our fiducial analysis method.

To validate our analysis method, we perform the following test in a similar way to what we do in the actual analysis. In this test, we keep the observed shear invariant, but assume that there is a bias in the mean redshift of source galaxies inferred from their photo-z's, by an amount Δz_{ph}^{in}. We assume that the "estimated" redshift distribution, denoted as $p_s(z)$, is given by a shift of the true distribution, $p_s(z)$, as

$$p_s(z) = p_s^{true}(z - \Delta z_{ph}^{in}). \tag{A1}$$

That is, $p_s(z + \Delta z_{ph}) = p_s^{true}(z)$, recovering the true distribution, if $\Delta z_{ph} = \Delta z_{ph}^{in}$. This Δz_{ph} is our parametrization

of the systematic photo-z error [Eq. (18)]. For our test we take $\Delta z_{\rm ph}^{\rm in} = -0.2$. Here $\Delta z_{\rm ph}^{\rm in} = -0.2$ is almost 2σ away from the Gaussian prior of $\Delta z_{\rm ph}$, $\mathcal{N}(-0.05, 0.09)$ used in our analysis. Hence this test gives the worst-case scenario for the impact of the photo-z bias error.

For our weak-lensing observables, a systematic error in the estimated redshift distribution, $p(z)$, causes a biased estimate of the excess surface mass density of

$$\widehat{\Delta\Sigma} = \frac{\langle\Sigma_{\rm cr}^{-1}\rangle^{-1}}{\langle\Sigma_{\rm cr}^{-1}\rangle_{\rm true}^{-1}}\Delta\Sigma_{\rm true}, \tag{A2}$$

where $\langle\Sigma_{\rm cr}^{-1}\rangle$ is the "estimated" average of the critical surface mass density with $p_s(z)$ in the ensemble average sense [see Eq. (16) in More *et al.* [17]], $\langle\Sigma_{\rm cr}^{-1}\rangle_{\rm true}$ is the true value computed with $p_s^{\rm true}(z)$, and $\Delta\Sigma_{\rm true}$ is the true excess surface mass density. In this way, we generate a synthetic data vector of $\Delta\Sigma$ including the effect of photo-z errors. The cosmic shear correlation functions $\xi_\pm$ are invariant, and we do not change the synthetic data vector of $\xi_\pm$ in our test. However, the theoretical model of $\xi_\pm$ for a given cosmology is biased because the model assumes an input source redshift distribution, i.e., $p(z)$. Then we assess whether our analysis method can recover the input S_8 and other parameters including $\Delta z_{\rm ph}$; if our calibration method works perfectly, the best-fit model should give $\Delta z_{\rm ph} = \Delta z_{\rm ph}^{\rm in}$. To estimate the impact of source redshift error, we also study how the S_8 value is biased *if* we employ the informative, narrower Gaussian prior of $\Delta z_{\rm ph}$ around $\Delta z_{\rm ph} = 0$, i.e. $\mathcal{N}(0, 0.1)$. Finally, and for completeness, we also perform the test using a flat prior, $\mathcal{U}(-1, 1)$.

d. PSF model

To model the PSF systematic effects on cosmic shear correlations ($\xi_\pm$), we take into account the PSF modeling error and PSF leakage based on the second moments of the PSF [Eq. (27)] in our model. The HSC-Y3 cosmic shear papers (Li *et al.* [18] and Dalal *et al.* [19]) accompanying this paper, used a more sophisticated, accurate model of PSF systematics than we do; their model incorporates terms depending on the fourth moment of the PSF following Zhang *et al.* [54], while we will only include the second-moment terms. In this paper, we use HSC source galaxies at high redshifts, $z \gtrsim 0.75$, where the lensing efficiency is higher, and therefore the impact of PSF systematics on the cosmic shear signal should be smaller than for the lower-redshift source galaxies used in the cosmic shear tomography analysis. Nevertheless we validate our method as follows.

Using the method in Zhang *et al.* [54], we measured the second and fourth moment PSF systematics terms for the HSC source galaxy sample used in this paper. We then generated a mock data vector of cosmic shear signal ($\xi_\pm$), contaminated with these PSF systematics, and then assessed whether our analysis method using the second moment PSF model can recover the input S_8 value.

2. Results of model validation tests

Figure 8 shows the results of the validation tests of our model and method as outlined above and in Table III. Here we compare the mode values of the cosmological parameters and the photo-z error parameter $\Delta z_{\rm ph}$ between our baseline analysis and the various analyses using subsets of our data and mock data contaminated with various kinds of systematics. For the analysis with superscript $*$, we run the large-scale analysis to the synthetic data using the informative prior on $\Delta z_{\rm ph}$ taken from the posterior of the small-scale 3×2pt analysis [16] on the same synthetic data vector. This is our baseline analysis method that we use for the actual HSC-Y3 and SDSS data.

The top section of Fig. 8 shows the results obtained using subsets of the data vector with the baseline analysis method. If we use either the 2×2pt data vector ($\Delta\Sigma$ and $w_{\rm p}$) or the cosmic shear, the constraints on the cosmological parameters are degraded compared to the baseline 3×2pt analysis. In addition, this method yields a somewhat biased estimate of S_8. This might explain the larger value of S_8 in the HSC-Y1 large-scale 2×2pt analysis in Sugiyama *et al.* [6], compared to the S_8 value from the small-scale 2×2pt or the HSC-Y3 3×2pt analyses.

The second section of Fig. 8 shows the results of the validation tests obtained by applying the baseline analysis method to mock data vectors measured from different types of mock SDSS galaxies. Here we used the mock SDSS catalogs described by Miyatake *et al.* [14], where mock galaxies are populated into halos in N-body simulations using different models of galaxy-halo connection. Our baseline analysis recovers the input cosmological parameter, $\Omega_{\rm m}$ and S_8, within 0.5σ, except for the `assembly-`*b* and `assembly-`*b*`-ext` mocks. Hence the results give validation of our analysis method for most of the mock catalogs, if the SDSS galaxies follow the galaxy-halo connection as that simulated by these mock catalogs.

The assembly bias is one of the most important systematic effects in the galaxy-halo connection. From Fig. 8 one might conclude that the minimal bias model fails to pass the validation test using the assembly bias mocks. However, this is not so simple as explained below. First of all, we would like to note that the assembly bias mocks we use in the tests assume the overwhelmingly large assembly bias effects and therefore give the worst-case scenario, where the `assembly-`*b* and `assembly-`*b*`-ext` mocks have the greater amplitudes in the 2-halo term of $w_{\rm p}$ by a factor of 1.3 and 1.5, even though the assembly bias has not yet been detected at a high significance from the SDSS galaxies. The apparent failure of our method for the assembly bias mocks is due to the degeneracies between the photo-z error parameter $\Delta z_{\rm ph}$ and the cosmological parameters. In our

baseline method, we use the informative prior on $\Delta z_{\rm ph}$ taken from the small-scale 3×2pt analysis of Miyatake *et al.* [16], which uses the uninformative flat prior $\Pi(\Delta z_{\rm ph})=\mathcal{U}(-1,1)$ to minimize the impact of the unknown source redshift uncertainty. To being with, the small-scale 3×2pt analysis fails to reproduce both the input cosmological parameters (e.g., S_8) and the input photo-z error parameter ($\Delta z_{\rm ph}=0$) for these synthetic data from the assembly bias mocks, because the small-scale analysis is severely affected by the assembly bias effect due to a violation in the simple scaling relation of galaxy bias amplitude with the host halo masses. On top of this, the small-scale analysis suffers from the parameter degeneracies due to a positive correlation between S_8 and $\Delta z_{\rm ph}$. For these reasons, the prior information of $\Delta z_{\rm ph}$ delivered from the small-scale 3×2pt analysis is biased in the first place. The row "`assembly-b-ext` w $\Pi(\Delta z_{\rm ph})=\mathcal{N}(0,0.1)$" shows the result obtained for our baseline method if we can use the informative Gaussian prior with mean around the true $\Delta z_{\rm ph}$ ($\Delta z_{\rm ph}=0$), where the prior width $\sigma(\Delta z_{\rm ph})=0.1$ roughly matches the precision of $\Delta z_{\rm ph}$ for the small-scale 3×2pt analysis. In this case, our method can nicely recover the input S_8 value, meaning that the minimal bias model can work even for the worst-case assembly bias scenario. However, this is not the case for the small-scale 3×2pt case; if such informative prior of $\Pi(\Delta z_{\rm ph}=\mathcal{N}(0,0.1)$ is employed for the small-scale analysis, S_8 is significantly biased due to the assembly bias effect. Thus, comparing the inferred S_8 values between the small- and large-scale 3×2pt analyses with the informative prior of $\Pi(\Delta z_{\rm ph})=\mathcal{N}(0,0.1)$ can be used as a flag of the possible assembly bias effect. For the actual HSC-Y3 and SDSS data, we did not find a significant shift in the S_8 values for the analyses using $\Pi(\Delta z_{\rm ph})=\mathcal{N}(0,0.1)$.

There is another diagnostic to flag the assembly bias effect in an actual analysis. The large-scale 3×2pt analysis is less affected by the assembly bias effect, even though the amount of the bias depends on the prior choice of $\Delta z_{\rm ph}$ as we discussed above. Hence, we can flag the significant assembly bias effect by comparing the S_8 values estimated from the large-scale and small-scale 3×2pt analyses. The right panel of Fig. 7 shows this test. The histogram is from the noisy 100 mock data where we assume that the simulated data is not affected by the assembly bias effect (i.e., no assembly bias simulations). The two arrows denote the S_8 differences expected from the mock data that are simulated from the assembly bias mocks we used above. The measured S_8 difference is quite consistent with the noisy mock data. With the statistical power of the HSC-Y3 data, we cannot conclude that our results are not contaminated by the assembly bias effect that is as large as simulated in the `assembly-b` mock, but the probability that our results are contaminated by the assembly bias effect as large as the `assembly-b-ext` mock is quite unlikely (at a 2σ level). Another rationale that we found after unblinding the HSC-Y3 cosmology results, although not objective, is a nice agreement between the S_8 values from the small-scale 3×2pt analyses and the cosmic shear analyses in Li *et al.* [18] and Dalal *et al.* [19]. If the SDSS galaxies are significantly contaminated by the assembly bias, this agreement is not guaranteed.

The third section in Fig. 8 tests the `halofit` model which we use to compute the cosmic shear prediction in our analysis method. The row "HMCode v2015 (DM only)" denotes the result for the mock cosmic shear data where baryonic effects are set to zero (i.e., $A_{\rm bary}=3.13$) Hence, shifts in the cosmological parameters between our baseline analysis and "HMCode v2015 (DM only)" are due to the difference in the nonlinear matter power spectra of `halofit` and the HMCode. Although $\Omega_{\rm m}$ and σ_8 show sizable shifts, the S_8 value is essentially identical in the two cases. We carried out tests with mock data generated using $A_{\rm bary}=2.8$ and 1.6 (`HMCode 2015`), and with $\log_{10}(T_{\rm AGN}/{\rm K})=7.3$ or 8.3 (`HMCode 2020`). Our baseline method recovers the S_8 value within the 0.33σ uncertainties for the mocks with $A_{\rm bary}=2.8$ (`HMCode 2015`) and $\log_{10}(T_{\rm AGN}/{\rm K})=7.3$ (`HMCode 2020`), and within the 1σ uncertainties for the mocks with $A_{\rm bary}=1.6$ (`HMCode 2015`) and $\log_{10}(T_{\rm AGN}/{\rm K})=8.3$ (`HMCode 2020`). Thus, these results confirm that our results are robust, given the cosmic shear scale cuts we have used ($\theta_{\rm min,+}=10^{0.8}$ arcmin and $\theta_{\rm min,-}=10^{1.5}$ arcmin).

The validation tests for the residual photo-z error parameter ($\Delta z_{\rm ph}$) shown in Fig. 8 are encouraging. Our baseline analysis method using the informative prior on $\Delta z_{\rm ph}$ taken from the posterior distribution of the small-scale 3×2pt analysis Miyatake *et al.* [16] nicely recovers the input S_8, even if the redshift source distribution inferred from the photo-z estimates is wrong, with a systematic error by $|\Delta z_{\rm ph}^{\rm in}|=0.2$. On the other hand, if we employ the informative Gaussian prior with mean around the wrong value $\Delta z_{\rm ph}=0$, i.e., $\Pi(\Delta z_{\rm ph})=\mathcal{N}(0,0.1)$, which is the prior used in the HSC-Y1 analysis, the estimate of S_8 is significantly biased compared to the input value, as can be found from the row "$\Delta z_{\rm ph}^{\rm in}=-0.2$, w/ $\Pi(\Delta_{\rm ph})=\mathcal{N}(0,0.1)$". If we employ the uninformative flat prior of $\Delta z_{\rm ph}$ for our large-scale 3×2pt analysis, we can recover the S_8 value, but the constraining power is significantly degraded, as shown in the row of "$\Delta z_{\rm ph}^{\rm in}=-0.2$, w/ $\Pi(\Delta_{\rm ph})=\mathcal{U}(-1,1)$". Hence we conclude that our baseline method is valid in the sense that it can safely recover the value of S_8 even if a systematic error in the mean redshift of HSC source galaxies is as large as 0.2. Figure 9 gives closer look at how the informative prior of the photo-z parameter from the small-scale analysis works in the large-scale analysis. The figure shows that S_8 strongly correlates with $\Delta z_{\rm ph}$. We again stress that, when we adopt an informative prior from the small-scale

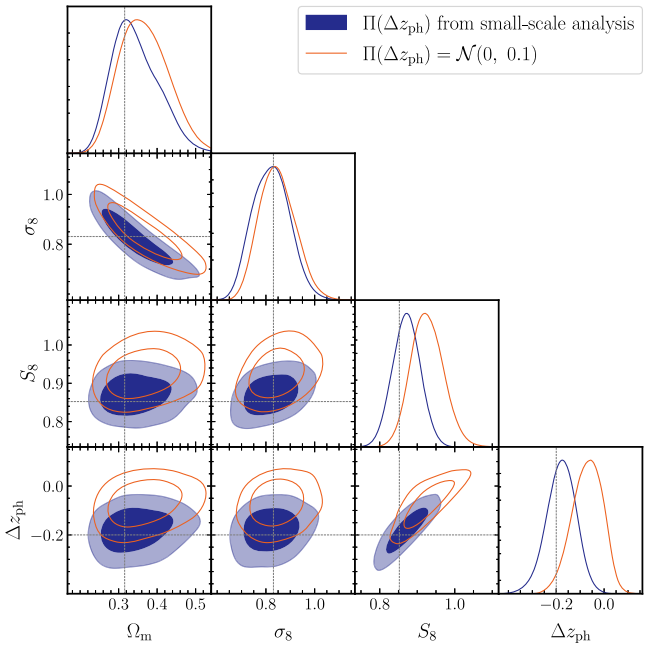

FIG. 9. Validation of the use of the $\Delta z_{\rm ph}$ prior taken from the small-scale 3×2pt analysis, which is our baseline analysis method. For this test, we use the synthetic data vector where we implemented the systematic error in the source redshift distribution modeled by $\Delta z_{\rm ph}^{\rm in} = -0.2$ (see Sec. A 1 c). The blue contours show the results obtained when analyzing the synthetic data vector with a prior taken from small-scale 3×2pt analysis method, while the orange contours show the results with an informative (but wrong!) prior $\mathcal{N}(0, 0.1)$.

analysis, which is correctly calibrated by the galaxy-galaxy lensing self-calibration [53], we recover the input value of S_8 within the statistical error.

Finally, the row labeled "PSF 4th" in Fig. 8 shows that our baseline analysis can recover the value of S_8 even if the cosmic shear signal is contaminated by fourth-moment PSF systematics. Thus we conclude that our model limited to second-moment PSF systematics is sufficient to model the cosmic shear signal.

APPENDIX B: A CORNER PLOT FOR ALL THE MODEL PARAMETERS

We present a corner plot for all the model parameters in Fig. 10. This figure shows the correlations between different model parameters. This figure can be used to infer how we can improve the parameter constraints with prior information or external data set in future studies.

APPENDIX C: INTERNAL CONSISTENCY TESTS

In this section, we detail the internal consistency tests performed in Sec. VI B. Table IV shows the statistics of model parameters, $\Omega_{\rm m}$, σ_8, and S_8, obtained from each analysis setup of the internal consistency tests. In this table, we report the estimate of parameters as

$$\text{mode}^{+34\%\ \text{upper}}_{-34\%\ \text{lower}}(\text{MAP}, \text{mean}), \tag{C1}$$

for ease of comparison with other papers. As noted in Sec. III D, the MAP value is estimated from the MC chain. The MAP obtained from the MC chain can be noisy and thus we should not take it as the robust estimate of MAP, but the difference between the MAP and the mode value gives an indication of how significant projection effects are in each case.

Figures 11–15 give contour diagrams of parameter constraints in the various internal consistency tests. The results of similar internal consistency tests are grouped and overplotted in each figure.

APPENDIX D: ROBUSTNESS OF PARAMETER SAMPLING

1. Nestcheck

In this section, we test the robustness of the parameter sampling by `MultiNest`. We use the `nestcheck` diagnostic [81] to test the convergence of the `MultiNest` chain. Figure 16 shows the result of the convergence test for the main cosmological parameters, $\Omega_{\rm m}$, σ_8, and S_8. In the top right panel, we can see that the chain covers sufficient posterior volume. The left panels show the uncertainty of the posterior distributions, estimated by bootstrapping the original MultiNest chain, and indicating that our estimate of the posterior distributions is robust.

As an additional test of convergence of our parameter estimate, Fig. 17 compares the result of the nested sampling by `MultiNest` [68] to the result of the Markov Chain Monte Carlo sampling method of the standard Metropolis algorithm [83]. The difference between the posterior estimates is almost negligible, and thus we conclude that our parameter inference by `MultiNest` is robust.

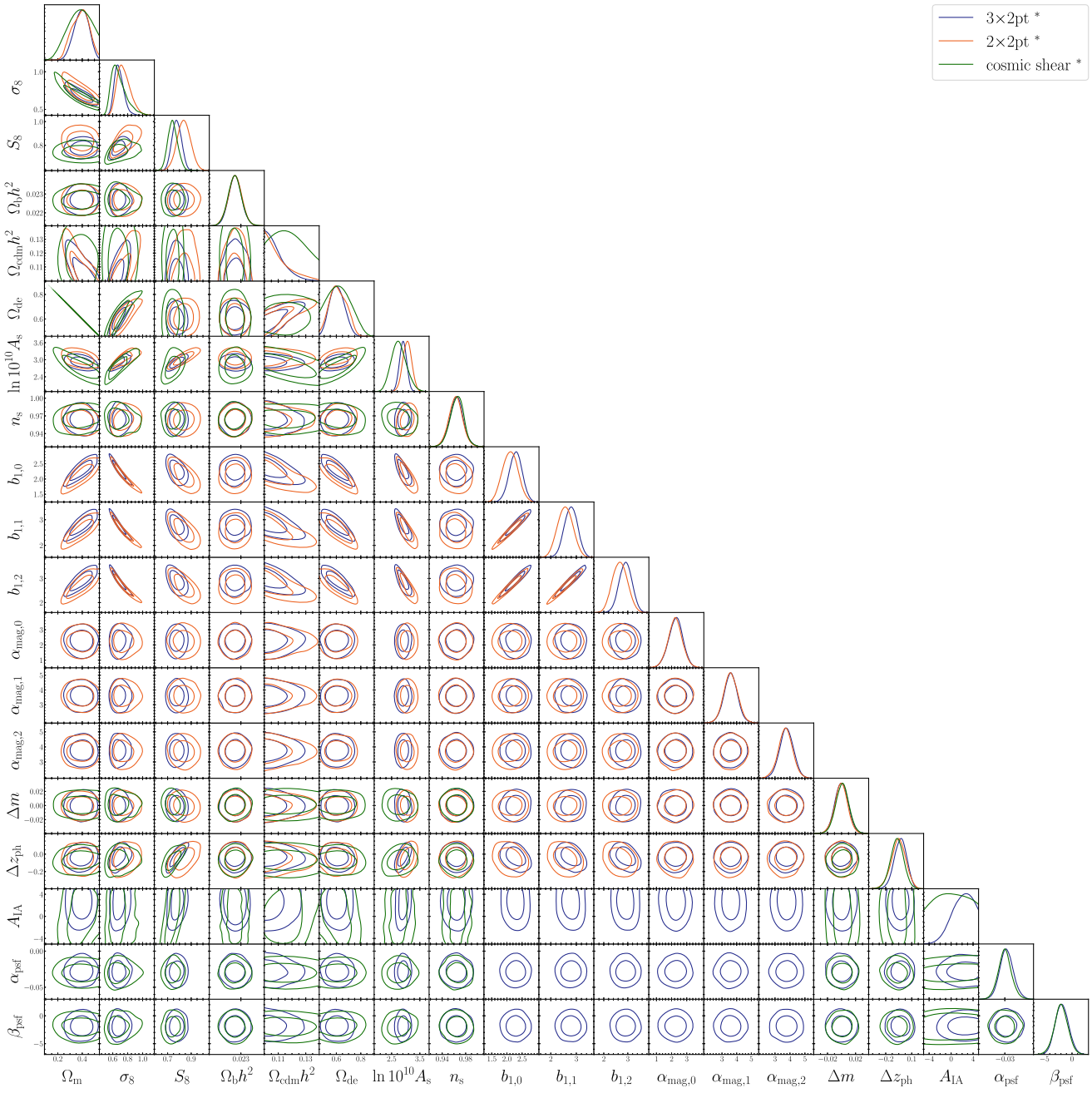

FIG. 10. Marginalized posterior distribution for all the model parameters with derived parameters, $\Omega_{\rm m}$, σ_8, and S_8. Here the parameter constraints are obtained from the baseline 3×2pt analysis (blue), the 2×2pt -only analysis (orange), and the cosmic shear alone analysis (green).

TABLE IV. Summary of the cosmological parameter constraints for $\Omega_{\rm m}$, σ_8, and S_8, obtained from our large-scale 3×2pt analysis of the HSC-Y3 and SDSS data. The estimates are presented in the format of mode$^{+34\%\ \rm upper}_{-34\%\ \rm lower}$(MAP, mean), where the mode is the peak of the marginalized posterior distribution, the credible interval is defined as the 68% highest density interval, the MAP is obtained from the MC chain with the highest posterior value, and the mean is defined as the parameter means with respect to the posterior. The analysis setup for each row is summarized in Table II. The analyses with superscript $*$ denote an analysis using the informative prior on $\Delta z_{\rm ph}$, given by $\Pi(\Delta z_{\rm ph})=\mathcal{N}(-0.05,0.09)$, taken from the small-scale 3×2pt analysis in Miyatake *et al.* [16], and the analysis with superscript † denotes the result using the informative Gaussian prior $\Pi(\Delta z_{\rm ph})=\mathcal{N}(0,0.1)$.

	$\Omega_{\rm m}$	σ_8	S_8
3×2pt*	$0.401^{+0.056}_{-0.064}(0.394,0.393)$	$0.666^{+0.069}_{-0.051}(0.705,0.685)$	$0.775^{+0.043}_{-0.038}(0.808,0.777)$
2×2pt*	$0.408^{+0.053}_{-0.091}(0.420,0.385)$	$0.713^{+0.105}_{-0.068}(0.710,0.749)$	$0.837^{+0.057}_{-0.056}(0.841,0.838)$
cosmic shear*	$0.385^{+0.103}_{-0.092}(0.411,0.374)$	$0.629^{+0.114}_{-0.068}(0.671,0.684)$	$0.739^{+0.043}_{-0.040}(0.785,0.744)$
3×2pt, w/o LOWZ*	$0.373^{+0.080}_{-0.062}(0.376,0.384)$	$0.667^{+0.083}_{-0.059}(0.702,0.690)$	$0.767^{+0.046}_{-0.038}(0.785,0.771)$
3×2pt, w/o CMASS1*	$0.360^{+0.071}_{-0.061}(0.419,0.369)$	$0.674^{+0.080}_{-0.061}(0.651,0.694)$	$0.758^{+0.043}_{-0.039}(0.769,0.760)$
3×2pt, w/o CMASS2*	$0.424^{+0.060}_{-0.077}(0.446,0.408)$	$0.653^{+0.067}_{-0.058}(0.666,0.671)$	$0.772^{+0.044}_{-0.036}(0.812,0.775)$
2×2pt, w/o LOWZ*	$0.407^{+0.069}_{-0.091}(0.427,0.389)$	$0.721^{+0.102}_{-0.073}(0.703,0.752)$	$0.841^{+0.062}_{-0.057}(0.838,0.844)$
2×2pt, w/o CMASS1*	$0.314^{+0.087}_{-0.064}(0.352,0.332)$	$0.757^{+0.132}_{-0.096}(0.722,0.795)$	$0.816^{+0.071}_{-0.061}(0.782,0.820)$
2×2pt, w/o CMASS2*	$0.403^{+0.067}_{-0.090}(0.254,0.387)$	$0.721^{+0.129}_{-0.084}(0.973,0.766)$	$0.864^{+0.062}_{-0.075}(0.895,0.856)$
No photo-z error	$0.394^{+0.056}_{-0.068}(0.453,0.387)$	$0.691^{+0.060}_{-0.059}(0.647,0.704)$	$0.796^{+0.021}_{-0.022}(0.795,0.793)$
No shear error*	$0.394^{+0.058}_{-0.065}(0.466,0.388)$	$0.678^{+0.068}_{-0.057}(0.632,0.695)$	$0.785^{+0.038}_{-0.042}(0.787,0.783)$
No magnification bias error*	$0.404^{+0.059}_{-0.064}(0.400,0.398)$	$0.669^{+0.067}_{-0.055}(0.661,0.683)$	$0.781^{+0.040}_{-0.043}(0.764,0.780)$
No PSF error*	$0.407^{+0.057}_{-0.061}(0.394,0.401)$	$0.667^{+0.062}_{-0.054}(0.685,0.680)$	$0.781^{+0.039}_{-0.039}(0.786,0.780)$
No IA*	$0.396^{+0.063}_{-0.063}(0.392,0.393)$	$0.653^{+0.076}_{-0.047}(0.669,0.680)$	$0.774^{+0.034}_{-0.038}(0.765,0.771)$
Extreme IA*	$0.402^{+0.057}_{-0.062}(0.380,0.395)$	$0.668^{+0.068}_{-0.056}(0.707,0.688)$	$0.781^{+0.041}_{-0.039}(0.796,0.782)$
$R_{\rm max}=30h^{-1}$ Mpc*	$0.384^{+0.062}_{-0.063}(0.417,0.385)$	$0.676^{+0.072}_{-0.060}(0.660,0.692)$	$0.775^{+0.040}_{-0.039}(0.779,0.776)$
3×2pt, 2 cosmo*	$0.316^{+0.038}_{-0.036}(0.304,0.323)$	$0.757^{+0.058}_{-0.057}(0.808,0.758)$	$0.783^{+0.039}_{-0.042}(0.813,0.782)$
2×2pt, 2 cosmo*	$0.316^{+0.037}_{-0.037}(0.290,0.318)$	$0.830^{+0.068}_{-0.080}(0.874,0.830)$	$0.850^{+0.056}_{-0.058}(0.859,0.850)$
$\Delta z_{\rm ph}\sim\mathcal{U}(-1,1)$	$0.399^{+0.061}_{-0.064}(0.473,0.396)$	$0.687^{+0.079}_{-0.064}(0.679,0.703)$	$0.802^{+0.059}_{-0.061}(0.852,0.800)$
3×2pt†	$0.406^{+0.053}_{-0.067}(0.490,0.397)$	$0.686^{+0.070}_{-0.054}(0.640,0.703)$	$0.802^{+0.042}_{-0.043}(0.819,0.801)$
2×2pt†	$0.398^{+0.067}_{-0.083}(0.287,0.380)$	$0.732^{+0.115}_{-0.079}(0.912,0.776)$	$0.856^{+0.066}_{-0.057}(0.892,0.860)$
cosmic shear†	$0.419^{+0.096}_{-0.088}(0.531,0.393)$	$0.626^{+0.111}_{-0.058}(0.569,0.677)$	$0.757^{+0.046}_{-0.047}(0.757,0.759)$
XMM ($\sim$33 deg^2)*	$0.387^{+0.062}_{-0.073}(0.357,0.378)$	$0.618^{+0.085}_{-0.071}(0.678,0.640)$	$0.711^{+0.072}_{-0.074}(0.739,0.712)$
GAMA15H ($\sim$41 deg^2)*	$0.338^{+0.073}_{-0.071}(0.356,0.348)$	$0.719^{+0.118}_{-0.091}(0.752,0.749)$	$0.793^{+0.075}_{-0.066}(0.819,0.794)$
HECTOMAP ($\sim$43 deg^2)*	$0.409^{+0.060}_{-0.076}(0.426,0.395)$	$0.673^{+0.095}_{-0.067}(0.678,0.706)$	$0.798^{+0.067}_{-0.066}(0.807,0.800)$
GAMA09H ($\sim$78 deg^2)*	$0.414^{+0.060}_{-0.065}(0.443,0.404)$	$0.650^{+0.070}_{-0.058}(0.650,0.668)$	$0.764^{+0.057}_{-0.051}(0.790,0.769)$
VVDS ($\sim$96 deg^2)*	$0.409^{+0.060}_{-0.076}(0.426,0.395)$	$0.673^{+0.095}_{-0.067}(0.678,0.706)$	$0.798^{+0.067}_{-0.066}(0.807,0.800)$
WIDE12H ($\sim$121 deg^2)*	$0.389^{+0.059}_{-0.072}(0.404,0.378)$	$0.631^{+0.084}_{-0.060}(0.662,0.659)$	$0.727^{+0.053}_{-0.051}(0.768,0.731)$
DEMPZ & WX*	$0.404^{+0.052}_{-0.069}(0.422,0.390)$	$0.653^{+0.071}_{-0.048}(0.641,0.677)$	$0.763^{+0.042}_{-0.035}(0.760,0.765)$
MIZUKI*	$0.415^{+0.057}_{-0.058}(0.407,0.409)$	$0.655^{+0.057}_{-0.050}(0.667,0.667)$	$0.772^{+0.036}_{-0.032}(0.776,0.774)$
DNNZ*	$0.403^{+0.059}_{-0.071}(0.400,0.390)$	$0.678^{+0.088}_{-0.057}(0.677,0.709)$	$0.796^{+0.050}_{-0.045}(0.782,0.799)$

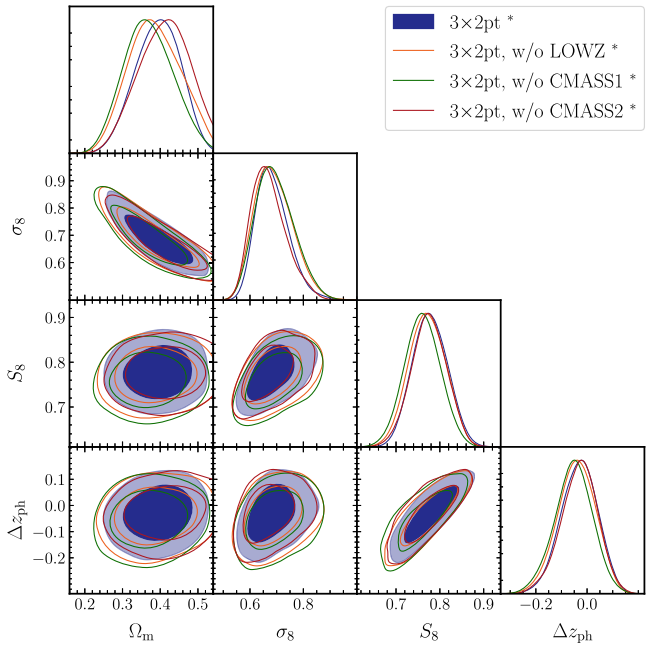

FIG. 11. Cosmological constraints with 3 × 2pt but removing a single lens redshift bin from each analysis.

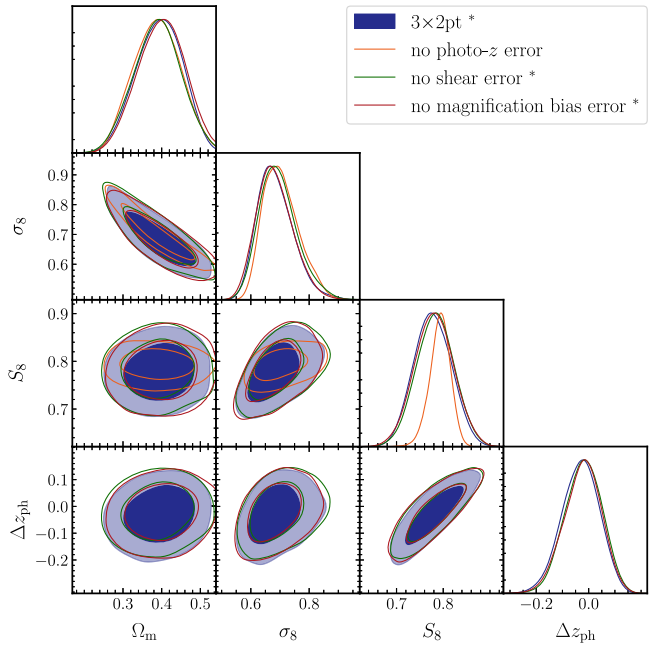

FIG. 13. Cosmological constraints with 3 × 2pt but fixing one of the nuisance parameters to zero.

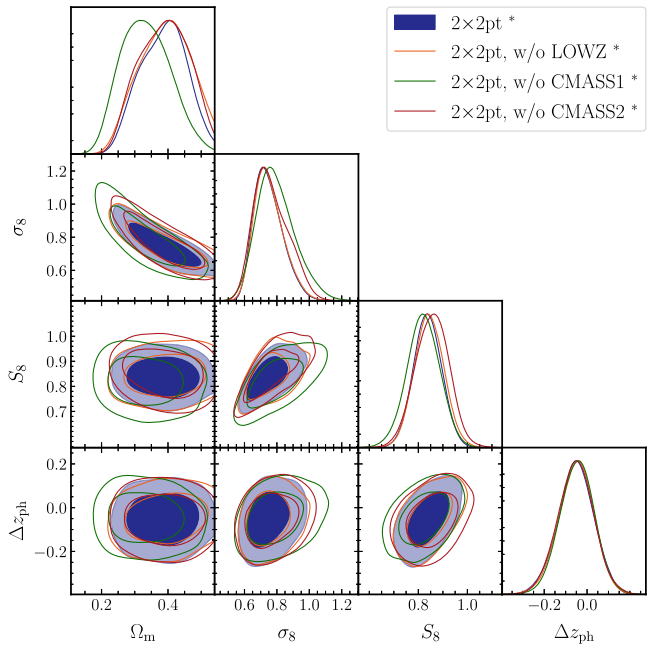

FIG. 12. Cosmological constraints with 2 × 2pt but removing a single lens redshift bin from each analysis.

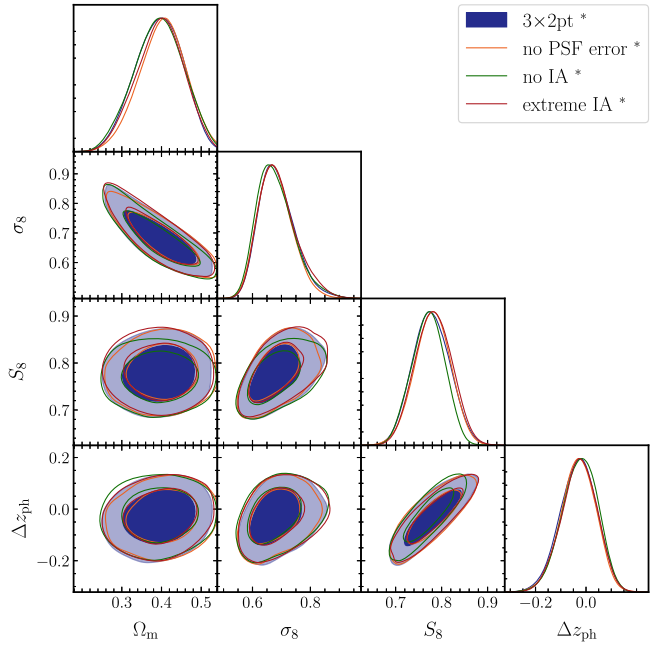

FIG. 14. Cosmological constraints with 2 × 2pt but fixing the cosmic shear related nuisance parameters to some fiducial values. In "no PSF error", we fix α_{psf} and β_{psf} to the center of the prior. In the "no IA" case, we fix $A_{IA} = 0$, while we set $A_{IA} = 5$ in the "extreme IA" case.

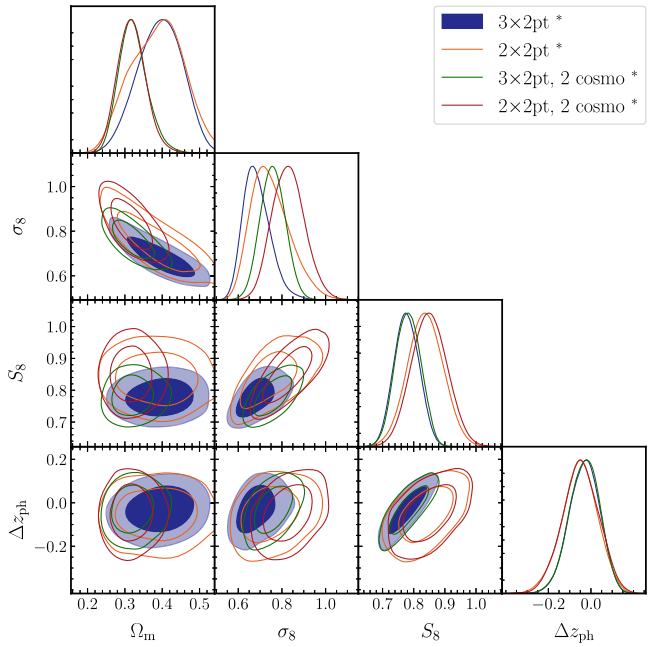

FIG. 15. Cosmological constraints with 2×2pt but fixing n_s and $\omega_{cdm} \equiv \Omega_{cdm} h^2$ to the best-fit value of [9], and $\omega_b \equiv \Omega_b h^2$ to the best fit of BBN [65–67].

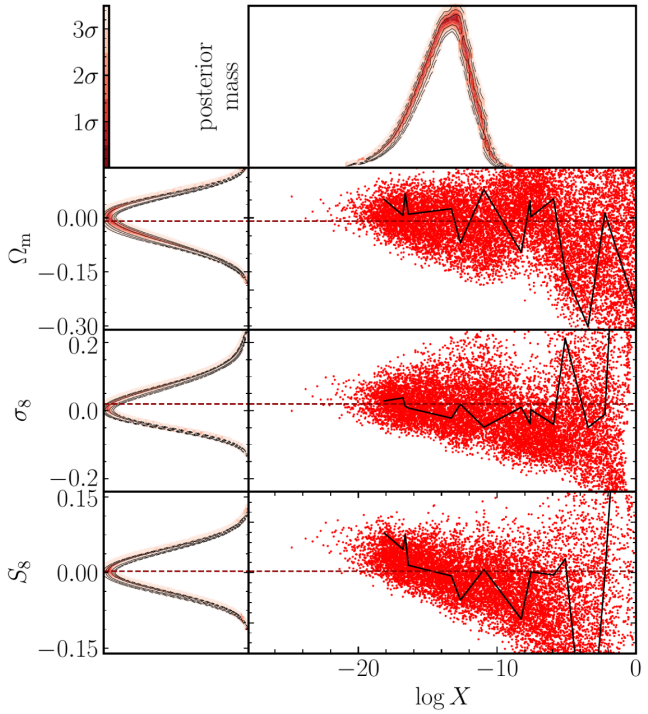

FIG. 16. The result of `nestcheck` [82] for the baseline chain, sampled in the real data analysis. The top panel shows the posterior volume as a function of the prior volume, X. The left panels show the uncertainty of the posterior distribution from an input nested sampling chain, where the uncertainty is estimated by bootstrapping the chain.

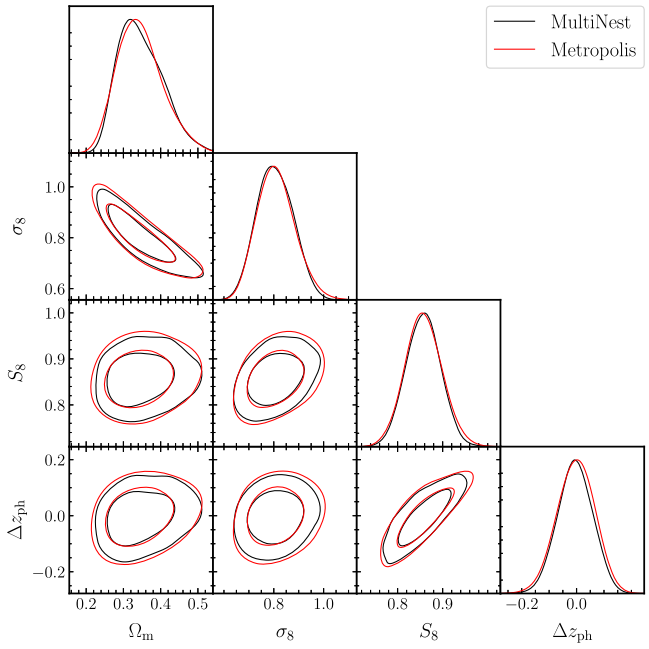

FIG. 17. The comparison of posterior estimates from the nested sampling by `MultiNest` and the Markov Chain Monte Carlo sampling by the standard Metropolis algorithm.

[1] S. Miyazaki, Y. Komiyama, S. Kawanomoto, Y. Doi, H. Furusawa, T. Hamana, Y. Hayashi, H. Ikeda, Y. Kamata, H. Karoji, M. Koike, T. Kurakami, S. Miyama, T. Morokuma *et al.*, Publ. Astron. Soc. Jpn. **70**, S1 (2018).

[2] H. Aihara, N. Arimoto, R. Armstrong, S. Arnouts, N. A. Bahcall, S. Bickerton, J. Bosch, K. Bundy, P. L. Capak, J. H. H. Chan *et al.*, Publ. Astron. Soc. Jpn. **70**, S4 (2018).

[3] C. Hikage, M. Oguri, T. Hamana, S. More, R. Mandelbaum, M. Takada, F. Köhlinger, H. Miyatake, A. J. Nishizawa, H. Aihara, R. Armstrong, J. Bosch, J. Coupon, A. Ducout *et al.*, Publ. Astron. Soc. Jpn. **71**, 43 (2019).

[4] T. Hamana, M. Shirasaki, S. Miyazaki, C. Hikage, M. Oguri, S. More, R. Armstrong, A. Leauthaud, R. Mandelbaum, H. Miyatake, A. J. Nishizawa, M. Simet, M. Takada, H. Aihara *et al.*, Publ. Astron. Soc. Jpn. **72**, 16 (2020).

[5] H. Miyatake, S. Sugiyama, M. Takada, T. Nishimichi, M. Shirasaki, Y. Kobayashi, R. Mandelbaum, S. More, M. Oguri, K. Osato *et al.*, Phys. Rev. D **106**, 083520 (2022).

[6] S. Sugiyama, M. Takada, H. Miyatake, T. Nishimichi, M. Shirasaki, Y. Kobayashi, R. Mandelbaum, S. More, R. Takahashi, K. Osato *et al.*, Phys. Rev. D **105**, 123537 (2022).

[7] A. Porredon, M. Crocce, J. Elvin-Poole, R. Cawthon, G. Giannini, J. De Vicente, A. Carnero Rosell, I. Ferrero, E. Krause, X. Fang *et al.*, Phys. Rev. D **106**, 103530 (2022).

[8] C. Heymans, T. Tröster, M. Asgari, C. Blake, H. Hildebrandt, B. Joachimi, K. Kuijken, C.-A. Lin, A. G. Sánchez, J. L. van den Busch *et al.*, Astron. Astrophys. **646**, A140 (2021).

[9] N. Aghanim, Y. Akrami, M. Ashdown, J. Aumont, C. Baccigalupi, M. Ballardini, A. J. Banday, R. B. Barreiro, N. Bartolo, S. Basak, R. Battye, K. Benabed, J. P. Bernard *et al.* (Planck Collaboration), Astron. Astrophys. **641**, A6 (2020).

[10] R. X. Adhikari, L. A. Anchordoqui, K. Fang, B. S. Sathyaprakash, K. Tollefson, T. R. Lewis, K. Engel, A. Aboubrahim, O. Akarsu, Y. Akrami *et al.*, arXiv:2209.11726.

[11] N. Kaiser, Astrophys. J. Lett. **284**, L9 (1984).

[12] V. Desjacques, D. Jeong, and F. Schmidt, Phys. Rep. **733**, 1 (2018).

[13] S. Sugiyama, M. Takada, Y. Kobayashi, H. Miyatake, M. Shirasaki, T. Nishimichi, and Y. Park, Phys. Rev. D **102**, 083520 (2020).

[14] H. Miyatake, Y. Kobayashi, M. Takada, T. Nishimichi, M. Shirasaki, S. Sugiyama, R. Takahashi, K. Osato, S. More, and Y. o. Park, Phys. Rev. D **106**, 083519 (2022).

[15] F. Bernardeau, S. Colombi, E. Gaztañaga, and R. Scoccimarro, Phys. Rep. **367**, 1 (2002).

[16] H. Miyatake, S. Sugiyama, M. Takada, T. Nishimichi, X. chong Li, M. Shirasaki, S. More, Y. Kobayashi, A. J. Nishizawa, M. M. Rau *et al.*, arXiv:2304.00704.

[17] S. More, S. Sugiyama, H. Miyatake, M. M. Rau, M. Shirasaki, X. Li, A. J. Nishizawa, K. Osato, T. Zhang, M. Takada *et al.*, arXiv:2304.00703.

[18] X. Li, T. Zhang, S. Sugiyama, R. Dalal, M. M. Rau, R. Mandelbaum, M. Takada, S. More, M. A. Strauss, H. Miyatake *et al.*, arXiv:2304.00702.

[19] R. Dalal, X. Li, A. Nicola, J. Zuntz, M. A. Strauss, S. Sugiyama, T. Zhang, M. M. Rau, R. Mandelbaum, M. Takada *et al.*, arXiv:2304.00701.

[20] Y. Komiyama, Y. Obuchi, H. Nakaya, Y. Kamata, S. Kawanomoto, Y. Utsumi, S. Miyazaki, F. Uraguchi, H. Furusawa, T. Morokuma, T. Uchida, H. Miyatake, S. Mineo, H. Fujimori *et al.*, Publ. Astron. Soc. Jpn. **70**, S2 (2018).

[21] H. Furusawa, M. Koike, T. Takata, Y. Okura, H. Miyatake, R. H. Lupton, S. Bickerton, P. A. Price, J. Bosch, N. Yasuda, S. Mineo, Y. Yamada, S. Miyazaki, F. Nakata *et al.*, Publ. Astron. Soc. Jpn. **70**, S3 (2018).

[22] S. Kawanomoto, F. Uraguchi, Y. Komiyama, S. Miyazaki, H. Furusawa, F. Finet, T. Hattori, S.-Y. Wang, N. Yasuda, and N. Suzuki, Publ. Astron. Soc. Jpn. **70**, 66 (2018).

[23] R. Mandelbaum, H. Miyatake, T. Hamana, M. Oguri, M. Simet, R. Armstrong, J. Bosch, R. Murata, F. Lanusse, A. Leauthaud *et al.*, Publ. Astron. Soc. Jpn. **70**, S25 (2018).

[24] R. Mandelbaum, F. Lanusse, A. Leauthaud, R. Armstrong, M. Simet, H. Miyatake, J. E. Meyers, J. Bosch, R. Murata, S. Miyazaki *et al.*, Mon. Not. R. Astron. Soc. **481**, 3170 (2018).

[25] J. Bosch, R. Armstrong, S. Bickerton, H. Furusawa, H. Ikeda, M. Koike, R. Lupton, S. Mineo, P. Price, T. Takata *et al.*, Publ. Astron. Soc. Jpn. **70**, S5 (2018).

[26] X. Li, H. Miyatake, W. Luo, S. More, M. Oguri, T. Hamana, R. Mandelbaum, M. Shirasaki, M. Takada, R. Armstrong *et al.*, Publ. Astron. Soc. Jpn. **74**, 421 (2022).

[27] A. J. Nishizawa, B.-C. Hsieh, M. Tanaka, and T. Takata, arXiv:2003.01511.

[28] M. Oguri, Mon. Not. R. Astron. Soc. **444**, 147 (2014).

[29] E. Medezinski, M. Oguri, A. J. Nishizawa, J. S. Speagle, H. Miyatake, K. Umetsu, A. Leauthaud, R. Murata, R. Mandelbaum, C. Sifón *et al.*, Publ. Astron. Soc. Jpn. **70**, 30 (2018).

[30] H. Miyatake, N. Battaglia, M. Hilton, E. Medezinski, A. J. Nishizawa, S. More, S. Aiola, N. Bahcall, J. R. Bond, E. Calabrese, S. K. Choi, M. J. Devlin, J. Dunkley, R. Dunner *et al.*, Astrophys. J. **875**, 63 (2019).

[31] S. Alam, F. D. Albareti, C. Allende Prieto, F. Anders, S. F. Anderson, T. Anderton, B. H. Andrews, E. Armengaud, É. Aubourg, S. Bailey *et al.*, Astrophys. J. Suppl. Ser. **219**, 12 (2015).

[32] K. S. Dawson, D. J. Schlegel, C. P. Ahn, S. F. Anderson, É. Aubourg, S. Bailey, R. H. Barkhouser, J. E. Bautista, A. r. Beifiori, A. A. Berlind, V. Bhardwaj, D. Bizyaev, C. H. Blake *et al.*, Astron. J. **145**, 10 (2013).

[33] K. N. Abazajian, J. K. Adelman-McCarthy, M. A. Agüeros, S. S. Allam, C. Allende Prieto, D. An, K. S. J. Anderson, S. F. Anderson, J. Annis, N. A. Bahcall *et al.*, Astrophys. J. Suppl. Ser. **182**, 543 (2009).

[34] J. E. Gunn, W. A. Siegmund, E. J. Mannery, R. E. Owen, C. L. Hull, R. F. Leger, L. N. Carey, G. R. Knapp, D. G. York, W. N. Boroski *et al.*, Astron. J. **131**, 2332 (2006).

[35] M. Fukugita, T. Ichikawa, J. E. Gunn, M. Doi, K. Shimasaku, and D. P. Schneider, Astron. J. **111**, 1748 (1996).

[36] J. A. Smith, D. L. Tucker, S. Kent, M. W. Richmond, M. Fukugita, T. Ichikawa, S.-i. Ichikawa, A. M. Jorgensen, A. Uomoto, J. E. Gunn *et al.*, Astron. J. **123**, 2121 (2002).

[37] M. Doi, M. Tanaka, M. Fukugita, J. E. Gunn, N. Yasuda, Ž. Ivezić, J. Brinkmann, E. de Haars, S. J. Kleinman, J. Krzesinski *et al.*, Astron. J. **139**, 1628 (2010).

[38] D. J. Eisenstein, D. H. Weinberg, E. Agol, H. Aihara, C. Allende Prieto, S. F. Anderson, J. A. Arns, É. Aubourg, S. Bailey, E. Balbinot *et al.*, Astron. J. **142**, 72 (2011).
[39] C. P. Ahn, R. Alexandroff, C. Allende Prieto, S. F. Anderson, T. Anderton, B. H. Andrews, É. Aubourg, S. Bailey, E. Balbinot, R. Barnes *et al.*, Astrophys. J. Suppl. Ser. **203**, 21 (2012).
[40] H. Aihara, C. Allende Prieto, D. An, S. F. Anderson, É. Aubourg, E. Balbinot, T. C. Beers, A. A. Berlind, S. J. Bickerton, D. Bizyaev *et al.*, Astrophys. J. Suppl. Ser. **193**, 29 (2011).
[41] R. Lupton, J. E. Gunn, Z. Ivezić, G. R. Knapp, and S. Kent, in *Astronomical Data Analysis Software and Systems X*, Astronomical Society of the Pacific Conference Series Vol. 238, edited by J. Harnden, F. R., F. A. Primini, and H. E. Payne (2001), p. 269, arXiv:astro-ph/0101420.
[42] J. R. Pier, J. A. Munn, R. B. Hindsley, G. S. Hennessy, S. M. Kent, R. H. Lupton, and Ž. Ivezić, Astron. J. **125**, 1559 (2003).
[43] N. Padmanabhan, D. J. Schlegel, D. P. Finkbeiner, J. C. Barentine, M. R. Blanton, H. J. Brewington, J. E. Gunn, M. Harvanek, D. W. Hogg, Ž. Ivezić *et al.*, Astrophys. J. **674**, 1217 (2008).
[44] D. J. Schlegel, D. P. Finkbeiner, and M. Davis, Astrophys. J. **500**, 525 (1998).
[45] A. S. Bolton, D. J. Schlegel, É. Aubourg, S. Bailey, V. Bhardwaj, J. R. Brownstein, S. Burles, Y.-M. Chen, K. Dawson, D. J. Eisenstein *et al.*, Astron. J. **144**, 144 (2012).
[46] F. C. van den Bosch, S. More, M. Cacciato, H. Mo, and X. Yang, Mon. Not. R. Astron. Soc. **430**, 725 (2013).
[47] R. E. Smith, J. A. Peacock, A. Jenkins, S. D. M. White, C. S. Frenk, F. R. Pearce, P. A. Thomas, G. Efstathiou, and H. M. P. Couchman, Mon. Not. R. Astron. Soc. **341**, 1311 (2003).
[48] R. Takahashi, M. Sato, T. Nishimichi, A. Taruya, and M. Oguri, Astrophys. J. **761**, 152 (2012).
[49] C. M. Hirata, R. Mandelbaum, U. Seljak, J. Guzik, N. Padmanabhan, C. Blake, J. Brinkmann, T. Budávari, A. Connolly, I. Csabai *et al.*, Mon. Not. R. Astron. Soc. **353**, 529 (2004).
[50] A. Heavens, A. Refregier, and C. Heymans, Mon. Not. R. Astron. Soc. **319**, 649 (2000).
[51] S. Bridle and L. King, New J. Phys. **9**, 444 (2007).
[52] D. Huterer, M. Takada, G. Bernstein, and B. Jain, Mon. Not. R. Astron. Soc. **366**, 101 (2006).
[53] M. Oguri and M. Takada, Phys. Rev. D **83**, 023008 (2011).
[54] T. Zhang, X. Li, R. Dalal, R. Mandelbaum, M. A. Strauss, A. Kannawadi, H. Miyatake, A. Nicola, A. A. P. Malagón, M. Shirasaki *et al.*, arXiv:2212.03257.
[55] S. More, H. Miyatake, R. Mandelbaum, M. Takada, D. N. Spergel, J. R. Brownstein, and D. P. Schneider, Astrophys. J. **806**, 2 (2015).
[56] M. A. Troxel, N. MacCrann, J. Zuntz, T. F. Eifler, E. Krause, S. Dodelson, D. Gruen, J. Blazek, O. Friedrich, S. Samuroff *et al.*, Phys. Rev. D **98**, 043528 (2018).
[57] R. Mandelbaum, C. M. Hirata, U. Seljak, J. Guzik, N. Padmanabhan, C. Blake, M. R. Blanton, R. Lupton, and J. Brinkmann, Mon. Not. R. Astron. Soc. **361**, 1287 (2005).
[58] X. Fang, E. Krause, T. Eifler, and N. MacCrann, J. Cosmol. Astropart. Phys. 05 (2020) 010.
[59] A. J. S. Hamilton, Mon. Not. R. Astron. Soc. **312**, 257 (2000).
[60] M. Shirasaki, T. Hamana, M. Takada, R. Takahashi, and H. Miyatake, Mon. Not. R. Astron. Soc. **486**, 52 (2019).
[61] M. Shirasaki, M. Takada, H. Miyatake, R. Takahashi, T. Hamana, T. Nishimichi, and R. Murata, Mon. Not. R. Astron. Soc. **470**, 3476 (2017).
[62] J. Hartlap, P. Simon, and P. Schneider, Astron. Astrophys. **464**, 399 (2007).
[63] R. Takahashi, T. Hamana, M. Shirasaki, T. Namikawa, T. Nishimichi, K. Osato, and K. Shiroyama, Astrophys. J. **850**, 24 (2017).
[64] M. Takada and W. Hu, Phys. Rev. D **87**, 123504 (2013).
[65] E. Aver, K. A. Olive, and E. D. Skillman, J. Cosmol. Astropart. Phys. 07 (2015) 011.
[66] R. J. Cooke, M. Pettini, and C. C. Steidel, Astrophys. J. **855**, 102 (2018).
[67] N. Schöneberg, J. Lesgourgues, and D. C. Hooper, J. Cosmol. Astropart. Phys. 10 (2019) 029.
[68] F. Feroz, M. P. Hobson, and M. Bridges, Mon. Not. R. Astron. Soc. **398**, 1601 (2009).
[69] J. Buchner, A. Georgakakis, K. Nandra, L. Hsu, C. Rangel, M. Brightman, A. Merloni, M. Salvato, J. Donley, and D. Kocevski, Astron. Astrophys. **564**, A125 (2014).
[70] T. M. C. Abbott, M. Aguena, A. Alarcon, S. Allam, O. Alves, A. Amon, F. Andrade-Oliveira, J. Annis, S. Avila *et al.* (DES Collaboration), Phys. Rev. D **105**, 023520 (2022).
[71] Y. Park and E. Rozo, Mon. Not. R. Astron. Soc. **499**, 4638 (2020).
[72] M. Raveri and W. Hu, Phys. Rev. D **99**, 043506 (2019).
[73] http://dm.lsst.org.
[74] P. A. R. Ade, N. Aghanim, M. Arnaud, M. Ashdown, J. Aumont, C. Baccigalupi, A. J. Banday, R. B. Barreiro, J. G. Bartlett *et al.* (Planck Collaboration), Astron. Astrophys. **594**, A13 (2016).
[75] M. Vogelsberger, S. Genel, V. Springel, P. Torrey, D. Sijacki, D. Xu, G. Snyder, S. Bird, D. Nelson, and L. Hernquist, Nature (London) **509**, 177 (2014).
[76] A. Mead, S. Brieden, T. Tröster, and C. Heymans, Mon. Not. R. Astron. Soc. **502**, 1401 (2021).
[77] A. Mead, J. Peacock, C. Heymans, S. Joudaki, and A. Heavens, Mon. Not. R. Astron. Soc. **454**, 1958 (2015).
[78] J. Schaye, C. Dalla Vecchia, C. M. Booth, R. P. C. Wiersma, T. Theuns, M. R. Haas, S. Bertone, A. R. Duffy, I. G. McCarthy, and F. van de Voort, Mon. Not. R. Astron. Soc. **402**, 1536 (2010).
[79] I. G. McCarthy, J. Schaye, S. Bird, and A. M. C. Le Brun, Mon. Not. R. Astron. Soc. **465**, 2936 (2017).
[80] A. M. C. L. Brun, I. G. McCarthy, J. Schaye, and T. J. Ponman, Mon. Not. R. Astron. Soc. **441**, 1270 (2014).
[81] E. Higson, W. Handley, M. Hobson, and A. Lasenby, Mon. Not. R. Astron. Soc. **483**, 2044 (2019).
[82] E. Higson, J. Open Source Softwaare **3**, 916 (2018).
[83] N. Metropolis and S. Ulam, J. Am. Stat. Assoc. **44**, 335 (1949).